

# CLARE 2000

## CLARE 2000 : Cloud Lidar & Radar Experiments



**GKSS : M. Quante, D. Nagel, U. Maixner, H. Lemke**  
**IPSL : C. Tinel, A. Protat, V. Noel, J. Pelon, J. Testud**  
**INSU/DT : F. Blouzon, N. Grand, G. Penazzi**  
**KNMI : H. Bloemink, D. Donovan, A. Van Lammeren**  
**LAMP : C. Duroure**  
**Météo-France : M. P. Lefebvre**  
**MPI : M. Dreyer, S. Bakan**

**December 2002**

**J. Pelon and J. Testud coordinators**



## SUMMARY

|   |              |
|---|--------------|
| <b>1. Introduction</b>  | <b>p. 5</b>  |
| <b>2. PART 1 : BREST Campaign</b>   | <b>p. 6</b>  |
| <b>2.1 Meteorological situation</b>   | <b>p. 6</b>  |
| <b>2.2 Measurements performed</b>   | <b>p. 8</b>  |
| <b>2.3 Data Analysis</b>  | <b>p. 11</b> |
| <br>  |              |
| <b>3. PART 2 : BRETIGNY Campaign</b>  | <b>p. 23</b> |
| <b>3.1 Meteorological situation</b>   | <b>p. 23</b> |
| <b>3.2 Measurements performed</b>   | <b>p. 29</b> |
| <b>3.3 Data Analysis</b>  | <b>p. 31</b> |
| <br>  |              |
| <b>4. Conclusion</b>  | <b>p. 41</b> |
| <br>  |              |
| <b>5. References</b>  | <b>p. 43</b> |
| <br>  |              |
| <b>Annexes</b>  |              |
| <br>  |              |
| ANNEX A : Instrument characteristics : Ground-based (Phase 1)                         | p. 47        |
| <br>  |              |
| ANNEX B : Instrument characteristics :<br>Airborne Instruments (Phases 1 & 2)         | p. 53        |
| <br>  |              |
| ANNEX C : Retrieval of particle size and water content from<br>radar – lidar analysis | p. 56        |
| <br>  |              |
| ANNEX D : Retrieval of cloud dynamics   | p. 62        |



## 1- Introduction

A better knowledge of cloud properties has been identified as a mandatory step to improve the operational weather and climate change forecasts. In the framework of the future space missions devoted to the monitoring of the microphysical, radiative, and dynamical properties of clouds (CLOUDSAT/CALIPSO as part of the “AQUA-Train”, developed by NASA and CNES, and the Earth-CARE mission, resulting from a collaboration between ESA and NASDA), the combination of active systems such as a cloud radar and a backscatter lidar presents the potential to meet this requirement. Ground-based and airborne measurements have been identified as a first step to evaluate the impact of these new techniques to more accurately retrieve cloud properties.

Statistical relationships linking the measured signal to the cloud microphysical properties have been issued from the analysis of lidar (Platt et al., 1998) and radar data (Matrosov et al., 1992, 1998; Sassen and Liao, 1996; Fox and Illingworth, 1997, among others). They however show large dispersions due to the variability of cloud physical parameters. The combination of radar and lidar measurements offers It has been initiated using infrared laser sources at NOAA in the 90's (Intrieri et al., 1993), and have shown the potential of the combined analysis. Other synergies have been proposed between radar and infrared passive radiometry (Matrosov et al., 1992).

The CLARE'1998 campaign has been the first international campaign organised by ESA to study these synergies (ESA WPP-170, 2000). It has allowed the development of new algorithms and their first testing against in situ measurements. Different methods for retrieving ice water content and effective diameter have been tested and compared. They are based on a direct analytical approaches and numerical iterative analyses involving statistical relationships. The objectives of the CLARE 2000 campaign were to allow additional observations, and as for CLARE'1998 to derive the macrophysical (bottom and top of the cloud, vertical structure ...), microphysical (ice/liquid water content), radiative ( $r_e$ ), and dynamic properties of clouds, from the radar-lidar observations to further test algorithms and investigate the interaction between dynamic/microphysical/radiative processes.

This campaign was organised in two phases. Measurements for the two phases of the campaign have been taken in meteorological conditions related to the occurrence of stratiform clouds. They were mainly taken ahead of cold fronts where multi-level clouds where multi-layered cloud systems were analysed. Mixed phase clouds were mainly aimed at during this campaign.

In a first phase held in November 2000, the support of ESA has allowed to combine CLARE and CARL (CARL - Cloud Analysis by Radar and Lidar- is a European project supported by European Community within framework 5) observations in the Brest area. The second phase was held in Bretigny. The dual-beam Doppler cloud radar (RASTA, Radar Aéroporté et Sol pour la Télédétection des propriétés nuAgeuses) developed in the frame of the French Radar-Lidar (RALI) project by CNRS and CNES was implemented with the dual wavelength backscatter lidar (LEANDRE 1), onboard the Avion de Recherche Atmosphérique et de Télédétection (ARAT) in the two phases.

## 2- PART 1 : The BREST Campaign

### 2.1 Meteorological situation

During the November 2000 period the prevailing low centered on England at the beginning of the campaign lead to heavy rain situations during the first days. First favourable conditions for mid-level and upper cloud observations were obtained on November 10<sup>th</sup> as the main low has moved eastward, and as another system was approaching northern Europe (Figure 1a).

On 10 November 2000, in the lower tropospheric layers, a deep low was established over the Northern Atlantic. This resulted in the development of a westerly flow over the western and northern part of Europe (Figures 1 (a-b)). The transferred warm and moist air masses from Atlantic Ocean created a system of warm clouds, which covered the western part of Europe and later extended eastwards as shown from Meteosat data (Fig. 1b). The observed cloud structure was associated to the warm front as it reached western France, flights were made in the west-east axis as the cold front was approaching.

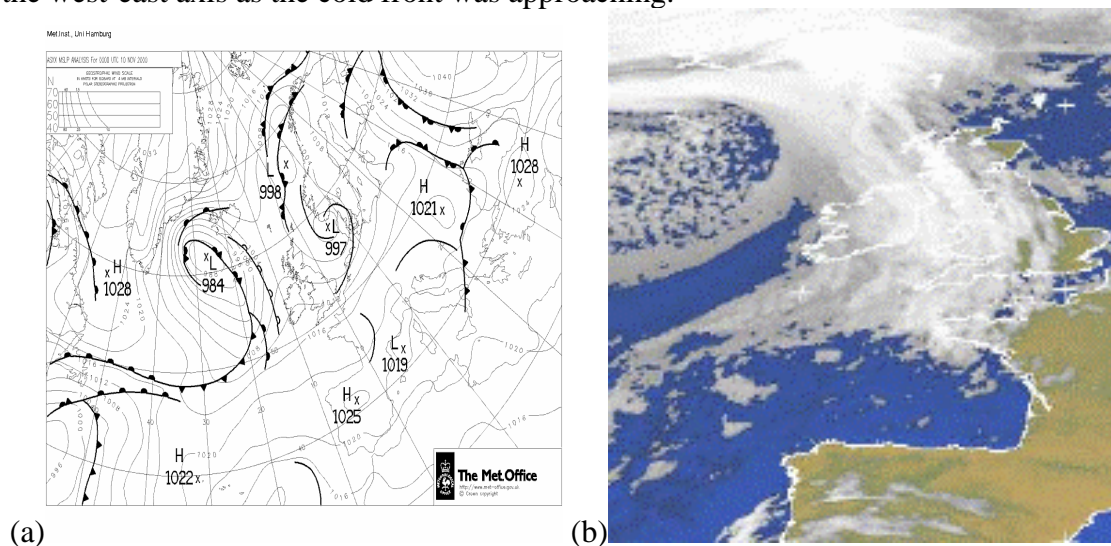


Figure 1 : a) Surface pressure analysis field (at 4 hPa intervals) from UK MetOffice, valid at 00:00 UTC 10 November 2000 and b) Meteosat IR image at 12 UTC.

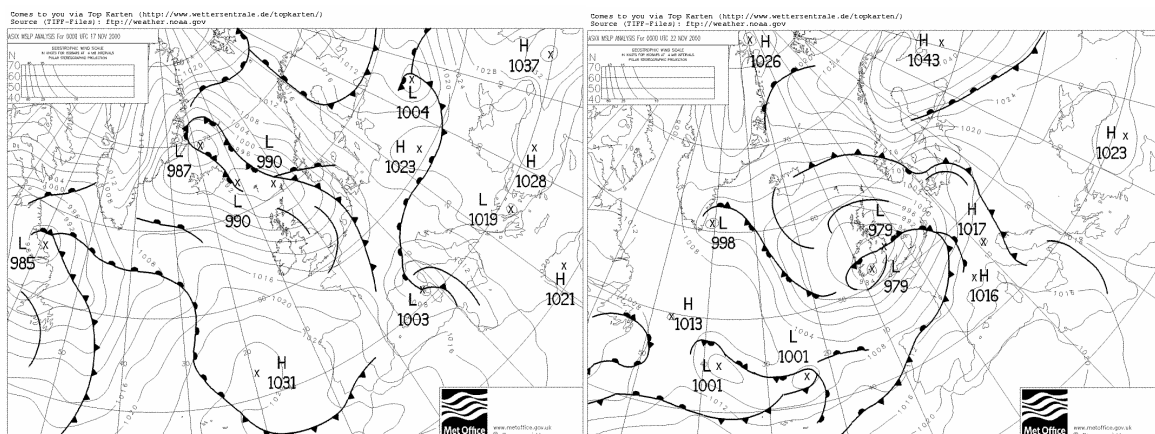


Figure 2 : Surface pressure analysis field (at 4 hPa intervals) from UK MetOffice, valid at 00:00 UTC on a) 16 November 2000 and b) 22 November 2000

After the passage of this front, which influenced marked the first week of operation, other favourable situations were met on the 17 and after the 20<sup>th</sup> November, as the low over England reinstalled. This is shown in Figure 2.

The outputs from meteorological models of the ECMWF and Meteo France (ARPEGE and ALADIN) were used to forecast potentially good situations and start the measurements. Hovmüller diagrams were plotted to define the forecasted cloud fraction over the Brest area. Figure 3 gives an example of the forecast at 120 h from the ECMWF starting at 12 UTC on 15 November and ARPEGE model starting at 00 UTC.

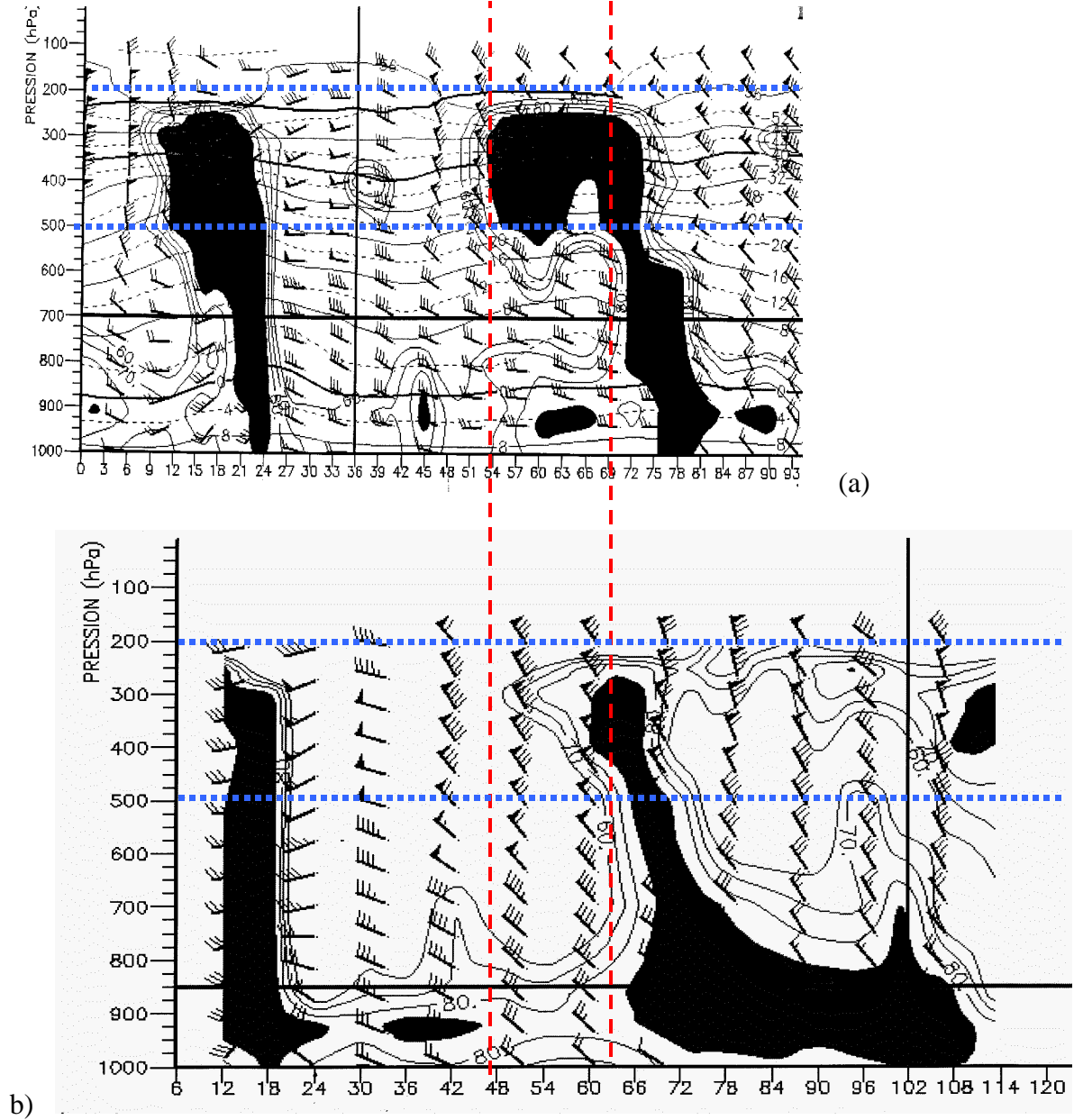


Figure 3 : a) Evolution diagram of forecasted moisture and wind over Brest over four days starting on 15 November 00 UTC b) same for ECMWF forecast starting at 12 UTC the same day (in this case 6 means 12 UTC).

One can see that the frontal passages are fairly well in phase, and the cloud top is consistent. However the moisture and thus the cloud occurrence at 500 hPa is very different. This is consistent with previous comparisons.

## **2.2 Measurements performed**

In this first phase measurements were taken between 6 November and 24 November 2000 in Brest. The Brest site was selected from the meteorology (frontal systems) and implementation of all instruments, and aircraft. A three weeks duration campaign has involved ground-based (GKSS radar, IPSL lidar) and airborne radar-lidar measurements.

Two aircraft were involved in the Brest campaign :

- the ARAT from CNRS/CNES/Météo-France/IGN for remote sensing
- the Merlin from Météo-France for in situ measurements

The ARAT carried the airborne backscatter lidar LEANDRE 1 from IPSL/SA and the new airborne cloud radar RASTA from IPSL/CETP. Both aircraft were equipped with in situ standard sensors including thermodynamics and radiometry (upward and downward visible and IR fluxes).

The Merlin IV was equipped for the campaign with the PMS sondes of GKSS for analysing size distribution and shapes of cloud particles in all clouds (FSSP, 2DP, 2DC).

Flight tracks were organised so that the end or start point of the flight tracks is the vertical of the ground-based measurements. The axis of the track being defined by the wind direction at cloud level. Track length is 30 nm which represents a measurement sequence of 10 minutes. This sequence is repeated up to ten times during a flight taking into account the turns. Details on the systems operated during this campaign are given in the Annex.

As seen in Table 1, some problems occurred during this first phase. The Merlin IV suffered from hydraulics problems which allowed measurements to be taken during three flights only. The emitter of the radar RASTA failed during the second flight. The KNMI ceilometer did not work properly after installation and had to be sent back for repair. However, very good results were obtained on November 10 which are further detailed in the analysis given hereafter.

**CARL campaign in Brest 6 November – 24 November 2000**

| Day (Nov) | GKSS Radar<br>MIRACLE | IPSL/SA Lidar<br>SLIM | KNMI Ceilom_r | KNMI IR Radiometer | KNMI Cloud Camera | MPI FTS OASIS | Merlin | ARAT IPSL/C ETPRA STA | ARAT IPSL/SA LEANDRE | Observations related to System operation   | Cloud height (500 hPa temperature) | Meteorological situation   | Quality/ Priority Index |
|-----------|-----------------------|-----------------------|---------------|--------------------|-------------------|---------------|--------|-----------------------|----------------------|--|------------------------------------|--|-------------------------|
| Mo 6      | -                     | -                     | -             | X                  | X                 | -             | -      | -                     | -                    | No ceilometer since 5/11<br>No depolarisation channel on radar<br>Miracle and lidar Slim | -                                  | Cold Front, rain   | -                       |
| Tu 7      | -                     | -                     | -             | X                  | X                 | -             | -      | X                     | X                    | -  | Variable                           | Occluded Front, rain   | -                       |
| We 8      | -                     | -                     | -             | X                  | X                 | -             | -      | -                     | -                    | -  | -                                  | Occluded Front, N. flow unstable, rain   | -                       |
| Th 9      | X                     | X                     | -             | X                  | X                 | -             | -      | -                     | -                    | -  | < 3 km and 5 to 7 km (-28 °C)      | Occluded front evolving NW flow, some mid-level clouds   | 4                       |
| Fr 10     | X                     | X                     | -             | X                  | X                 | -             | X      | X                     | X                    | Leandre acquisition problem (one leg).<br>Rasta failure at the end of ARAT flight        | < 2.5km and 3 to 9 km (-28 °C)     | Warm sector, mid and high level clouds   | 1                       |
| Sa 11     | -                     | -                     | -             | X                  | X                 | -             | -      | -                     | -                    | -  | -                                  | Pre-frontal situation :<br>Low level clouds, rain at 10 UTC, cold front passing                  | -                       |
| Su 12     | X                     | X                     | -             | X                  | X                 | -             | -      | -                     | X                    | Merlin Flight cancellation<br>Front wheel problem<br>parts from US needed<br>No flight   | <2.5 km and 6-10 km (-22 °C)       | End of cold front band, passing in the morning, middle and high level clouds on the western edge | 3                       |
| Mo 13     | X                     | X                     | -             | X                  | X                 | -             | -      | -                     | -                    | Depolarisation channel operating on Slim<br>Arrival of                                   | < 2km, 4km and 5-7 km (-25 °C)     | Northerly flow, occluded front, unstable, mid-level clouds prior to small cut-off low            | 4                       |

|       |   |   |   |   |   |   |   |   |   | MPI/FTS                                    |  |  |   |
|-------|---|---|---|---|---|---|---|---|---|--|--|--|---|
| Tu 14 | - | - | - | X | X | - | - | - | - | -  | -  | Northerly flow, occluded front, unstable                     | - |
| We 15 | X | X | - | X | X | X | - | - | X | -  | < 2 km, 3 to 7 km                              | Warm sector ahead of cold front                              | 2 |
| Th 16 | - | - | - | X | X | - | - | - | - | -  | -  |  | - |
| Fr 17 | X | X | - | X | X | X | - | - | X | ARAT flying back to Creil after mission    | <2 km, 7 to 10 km and then 4 to 7 km + 7-10 km | Warm front reaching Brest at 15 UTC thin cirrus and As after | 3 |
| Sa 18 | - | - | - | X | X | - | - | - | - | -  | -  | Warm sector, precipitations                                  | - |
| Su 19 | - | - | - | X | X | - | - | - | - | -  |  | Cold front , precipitations                                  | - |
| Mo 20 | - | - | X | X | X |   |   | - | - | Ceilometer re-installed Merlin operational |  |  | - |
| Tu 21 | - | - | X | X | X |   |   | - | - | -  |  |  | - |
| We 22 | X | X | X | X | X |   | X | - | - | No cloud over Brest                        |  | Warm front   | 3 |
| Th 23 | - | - | X | X | X |   | - | - | - | -  |  |  | - |
| Fr 24 | X | X | X | X | X |   | X | - | - | -  | <2 km, 7 to 10 km                              | Warm sector, some rain                                       | 2 |

Table 1 : Summary of Operation during phase 1 of CLARE 2000, instruments involved and observations (All times are UTC).

A complementary instrument was used to give additional information on the water and ice contents : the Nevzorov sonde. A specific implementation and dedicated tests were made before the campaign to install and use this instrument.

It was the first campaign for the IPSL/CETP radar RASTA. After the second flight, a failure of the emitter was observed and it was sent back to the US. Mechanical problems then occurred on the Merlin, which was kept to the ground 10 days waiting for spare parts. Three more flights were however made with the aircraft as detailed in Table 7. More details about the aircraft instrumentation are given in Annex.

## 2.3 Data Analysis

### 2.3.1 OASIS Data Analysis (MPI, Hamburg)

The measurements during CLARE2000 were performed mostly at daytime under non-raining conditions. The data set of more than 7600 single spectra consists of measurements of all cloud types and of clear sky conditions, as well. Even after reducing the continuous spectra to sets of 45 channels, there is a large amount of data remaining. In order to get some information about the data structure, multi-variate analysis methods, namely EOF and cluster analysis, were applied (Kendall, 1980; Morrison, 1990). The EOF (**E**mpirical **O**rtogonal **F**unction) analysis was used to determine inherent dependencies between the channels. Furthermore, it gives an idea about the number of independent parameters. But this number does not necessarily correspond to the real number of physically relevant parameters, since these do not need to be orthogonal, as the EOFs are. In fact, the main microphysical parameters of clouds modifying the downwelling radiation like optical depth, liquid or ice water content, effective particle radius and particle size distribution are not independent from each other. This must be regarded as a disadvantage of the EOF analysis. The cluster analysis was used to find out possible accumulations of spectra in the 45-dimensional data set. These accumulations may lead to an accurate cloud classification. Since the radiances in the TIR and the NIR region differ by a factor of 100, this must be taken into account in applying these methods.

The radiation transfer model SBDART (**S**anta **B**arbara **D**ISORT **A**tmospheric **R**adiation **T**ransfer, Ricchiazzi et al., 1998) was used for sensitivity studies. As mentioned by its name, it includes the DISORT (**D**IScrete **O**rdinate **R**adiation **T**ransfer, Stamnes et al., 1988) algorithm to simulate both the thermally emitted and the scattered solar radiation in a vertically inhomogeneous atmosphere. SBDART is a fast and easy-to-use tool since the input parameters can simply be modified by scripts, so that it can calculate sets of spectra in a short time. The FORTRAN77 code can be adopted to special needs like a personalized output. The possibility to calculate signals at specified wavenumbers is very useful to reduce the calculations to the center wavenumbers of the channels used in this study. The resolution of  $20 \text{ cm}^{-1}$  is more than sufficient for the NIR range, but, unfortunately, in the TIR range the channel bandwidth is commonly smaller than the provided resolution. That means, especially for some narrow TIR micro-windows, that the results are not very accurate. In order to retrieve microphysical parameters of the observed clouds, a model with higher resolution has to be used.

Figure 4 shows the result of the EOF analysis of the CLARE2000 spectra compared to the results for test measurements which were performed in March 1999 near Hamburg (Dreyer and Bakan, 2001). Due to the large spectral variability of the radiance values, the EOF

analysis was based on the correlation matrix instead of the covariance matrix. While the spectra at CLARE2000 result from single scans, the test measurement spectra are co-added from 12 scans. Both cases consist of spectra from clouds at all levels and of clear sky situations, too. The first EOF, which represents about 80 % of the variance, is apparently linked to the optical depth. The glitches around wavelengths of 1.5, 2 and 3  $\mu\text{m}$ , respectively, can be traced back to absorption of cloud water and cloud ice. It is remarkable, that in all cases the first four EOFs represent nearly 99 % of the total variance. Since they are clearly distinguished, they should not be neglected, although care has to be taken in interpreting them in terms of individual physical processes, as mentioned above.

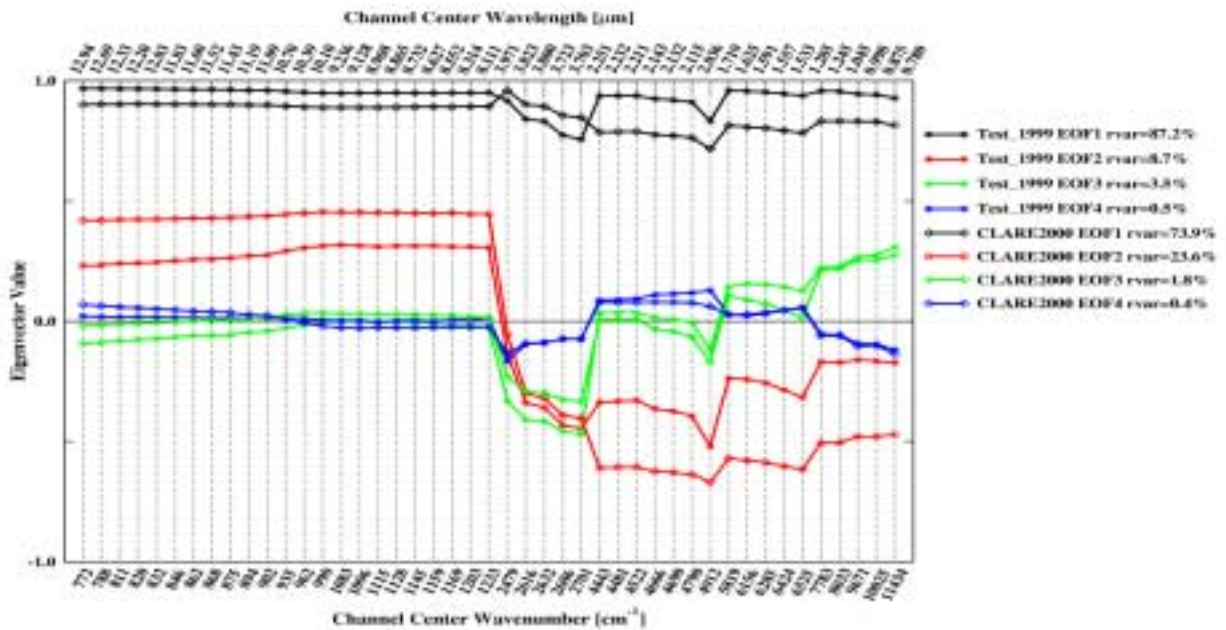


Figure 4: EOF analysis of all CLARE2000 spectra in comparison to test measurements.

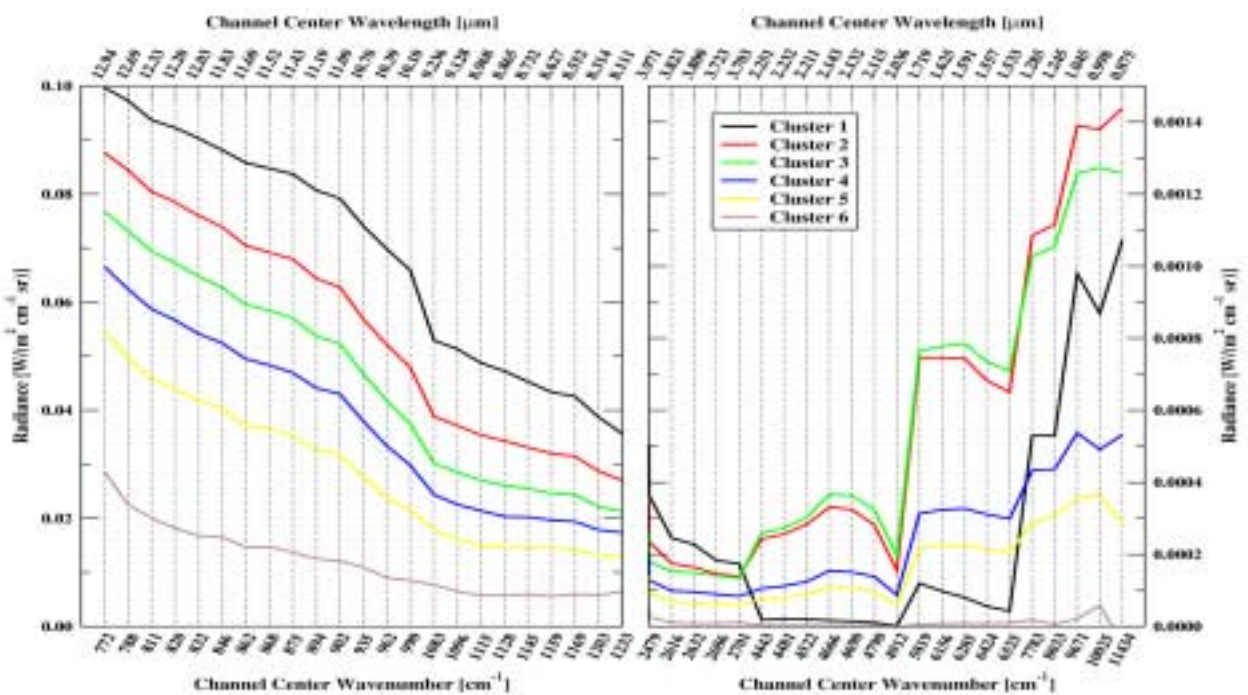


Figure 5 a: Cluster analysis of the CLARE2000 spectra.

A cluster analysis was performed on the complete data set, which results in a set of six clusters. Due to the spectral variability, the spectra are weighted with the vector of the maximum value of each channel. Figure 5a shows the resulting cluster center vectors. In the thermal infrared the radiance of the cluster centers increases monotonically with temperature of the cloud base and with cloud emissivity due to the optical depth, following the spectral behaviour of the Planck function. At wavenumbers larger than  $2400\text{ cm}^{-1}$  the measured radiance is strongly depending on the varying solar zenith angle, which leads to a variable radiance signal even under stationary cloud conditions. Therefore, the signal in this range has to be converted to a constant zenith angle before it can contribute to the cluster analysis result in a correct way. Obviously, the cluster analysis seems to be dominated by the TIR. Up to now, the ascertained clusters can not be associated uniquely to the simultaneously observed cloud types.

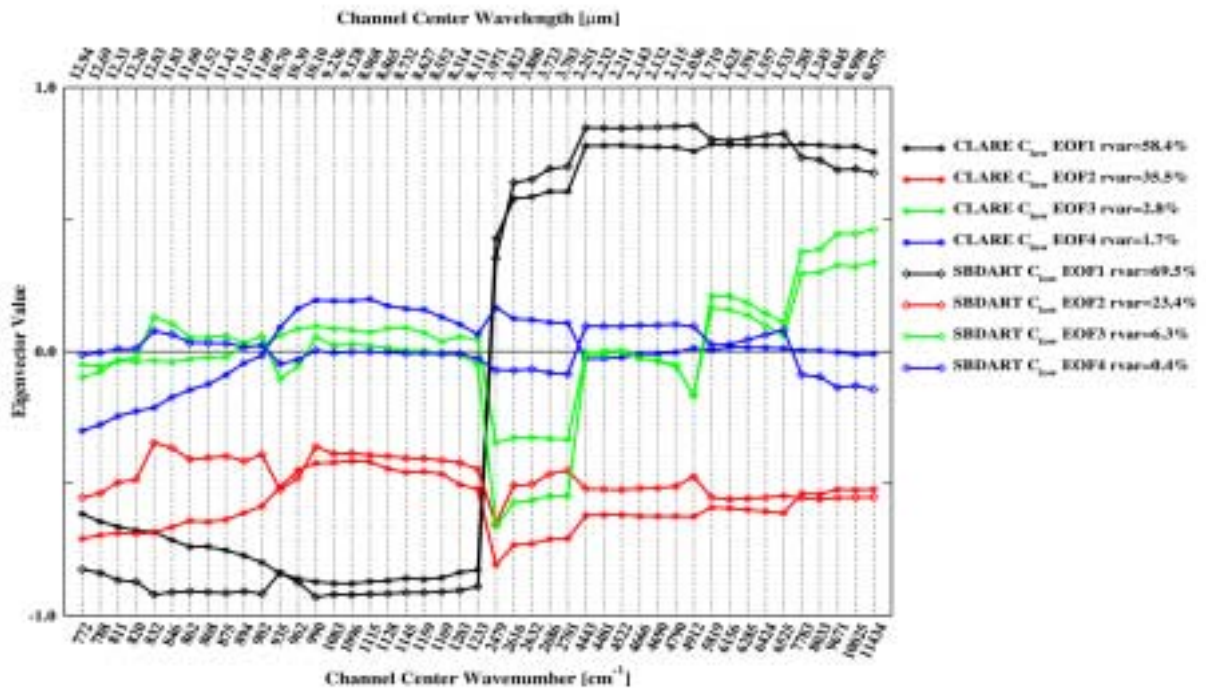


Figure 5b : EOF analysis of the CLARE2000 low cloud cluster spectra compared to simulated spectra of low clouds.

In Figure 5b the EOF of the cluster with the highest radiances in the thermal infrared region (cf. Fig. 4), which represents the lowest clouds, is compared to that of radiation transfer calculations using SBDART for low clouds with randomly varied microphysical and geometric parameters. Due to the low resolution of SBDART, the TIR EOFs of the simulated spectra are slightly disturbed compared to those of the measured signals. Nevertheless, the characteristic signatures stay discernible.

In general, the principal structure of the EOFs is very similar. In the TIR range all the first four EOFs are spectrally very smooth. Even if the third and fourth EOF have very small values, it is evident that they are changing their sign at wavenumbers around  $900\text{ cm}^{-1}$ . The behaviour in the NIR range is completely different from that of the TIR range. Regarding the NIR channel configuration (see annex), there are some larger gaps between the groups of

channels. Therefore, there are some characteristic differences between these groups. But there are also specific signatures inside of the groups as well, so it seems to be of advantage not to merge these channels in order to reduce both the amount of data and the noise level. Comparing Figures 5 and 3, the sign of the TIR range has interchanged, but the spectral signature itself remains unchanged. This spectral behaviour appears at all EOF analyses of data sets consisting only of clouds of higher optical depth, whereas the signature of Figure 3 is a typical result of analysing data including high clouds with low optical depth and clear-sky spectra, as well.

Both, the EOF and the cluster analysis are showing three different regimes. In the TIR range, there is a lot of redundant information, which is a clear result of the EOF analysis. The range of scattered solar radiation at wavenumbers larger than  $3000\text{ cm}^{-1}$  contains obviously a certain amount of additional information. But the signals in this range are strongly dependent on the varying solar zenith angle, which must be kept in mind during the data evaluation. The spectral range between  $2400$  and  $2700\text{ cm}^{-1}$  is influenced both by thermal and scattered solar radiation. Regarding the cluster centers in Figure 5, the signal of this range for cloudy conditions is clearly distinguishable from that of clear sky conditions, which are represented by cluster 6. Hence, this region may serve as an indicator for the purpose of cloud detection.

Concerning the results of the other participants of CLARE2000, only the geometrical parameters of clouds from the GKSS W-band radar MIRACLE have been used for simulations with SBDART up to now. Both, the data from the ground-based instruments and the airborne *in situ* measurements will be needed in future to validate our retrieved macro- and microphysical cloud parameters.

Our results clearly show the potential of multi-channel spectral analysis of the combined terrestrial and solar infrared spectral range for the determination of cloud properties. The measured spectra show a distinctly different spectral variation both, between the two spectral regions and within the regions itself, depending on the observed scene. This enables a discrimination and classification of various cloud types. The channels in the spectral range from  $2400$  to  $2700\text{ cm}^{-1}$  are influenced by both the thermal and the scattered solar radiation. Therefore, this range reacts especially sensitive to the appearance of clouds, so that it can be used for the discrimination between clear sky and cloudy spectra.

The combination of intervals of the whole spectrum into a set of micro-window channels leads to an averaging and therefore a noise reducing effect, so that the measurements can be carried out at fairly high temporal resolution without co-adding of spectra. Together with methods of multivariate analysis a certain cloud classification seems possible. Furthermore, we ultimately expect to be able to estimate microphysical cloud properties like effective radius, optical depth and liquid water content at useful accuracy by means of optimization techniques using radiative transfer models.

### **2.3.2 MIRACLE Radar Data Analysis (GKSS)**

The cloud structure observed by the GKSS radar emphasises that these two main cloud layers were fairly distinct below and above  $2\text{ km}$  as given in Fig.6.

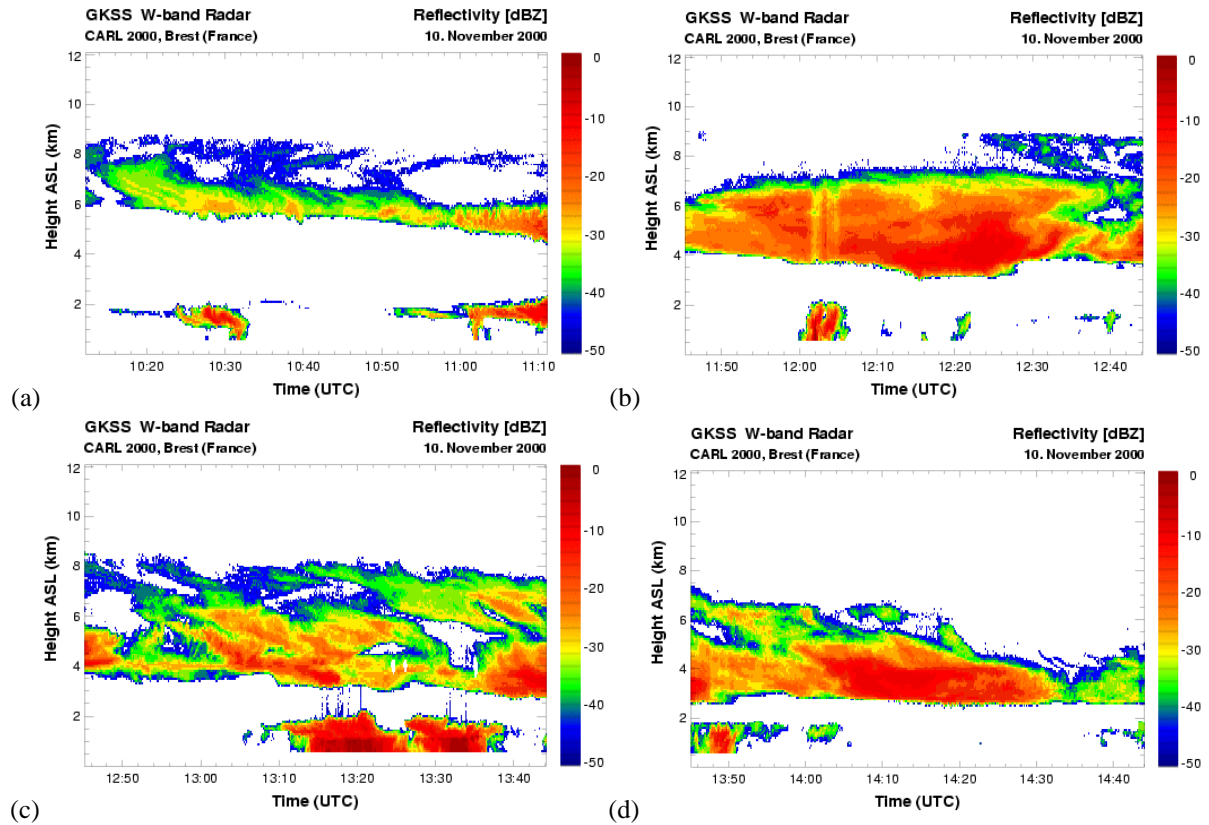


Figure 6 : Reflectivity measurements from the GKSS radar for November 10 2000

Cloud top reached an altitude of 9 km and cloud base was observed to decrease with time (up to 14 UTC) from 6 to 3 km, as upper level clouds were disappearing. Radar-lidar airborne measurements were performed between 12 and 13:40 UTC. One can see from the radar observations that it corresponds to three clouds bands two between 3 and 8 km and the third one below 2 km. The middle altitude cloud band was extending between 3 and 5 km, and the aircraft was flying at its top. In the lower cloud band precipitations are seen to occur at about an altitude of 1.2 km into the cloud, as seen from the melting layer evidencing the transition between mixed ice/water particles and rain (reflectivity and vertical speed) in radar data (Fig.32, and airborne data, not shown).

### 2.3.3 Ground-based lidar SLIM

As detailed in Table 1, lidar measurements with the mobile system SLIM have been performed throughout the whole period. As measurements were taken from the ground, water clouds were attenuating much of the signal preventing observing upper level clouds. This is clearly evidenced in Fig. 7 where only the base of the clouds can be detected when one compares with Fig 6 where radar measurements are reported.

On the 17 November, only few low level clouds were observed, which allowed to compare upper level cloud prediction and observation. Cloud forecast given by the Aladin model at the 20 km scale are reported in Fig. 8 a. This forecast is seen to correspond to the larger scale forecast from ARPEGE model given in Fig. 2.

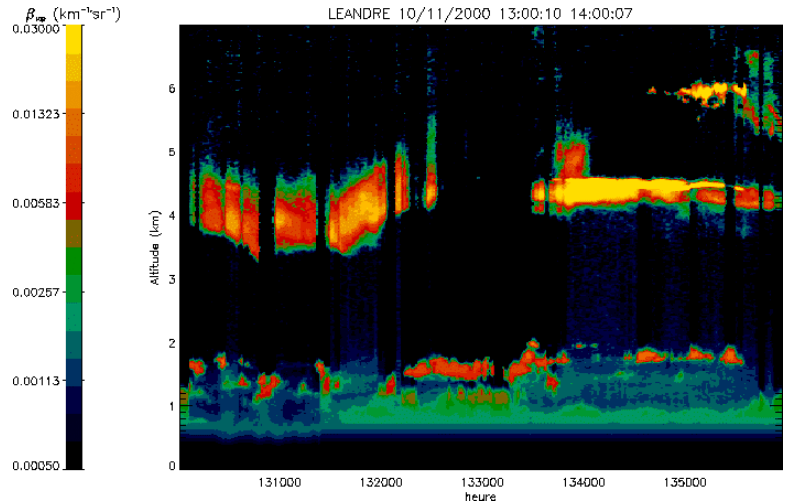


Figure 7 : Attenuated backscattering measured by the ground-based lidar SLIM at Brest on the 10 November 2000 between 13 and 14 UTC.

Results obtained in the flight time period with the ground-based lidar are reported in Figure 7. Observations correspond to the radar measurements reported in Figure 6. More low level clouds are detected by lidar. The cloud base undulation in the mid-level cloud layer is detected by both instruments, but its altitude variation is slightly different after 13:40UTC. This may be due to precipitations not detected by the lidar below the opaque cloud layer detected at 4 km. This layer is possibly presenting a higher liquid water content, strongly attenuating the lidar signal. Another example is given in Figure 8 for the 17 November 2000 over the whole day. The upper level cloud structure observed by lidar corresponds to the forecast given by Aladin model (Fig 8a), but the onset of cirrus clouds are seen to occur earlier in the evening. Some low level cloud features are detected in the moist layer identified by the model.

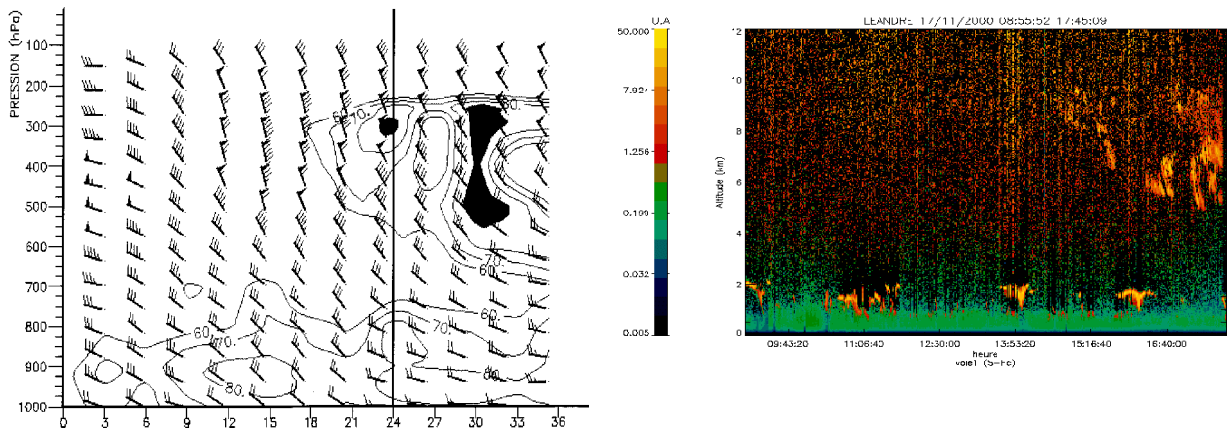
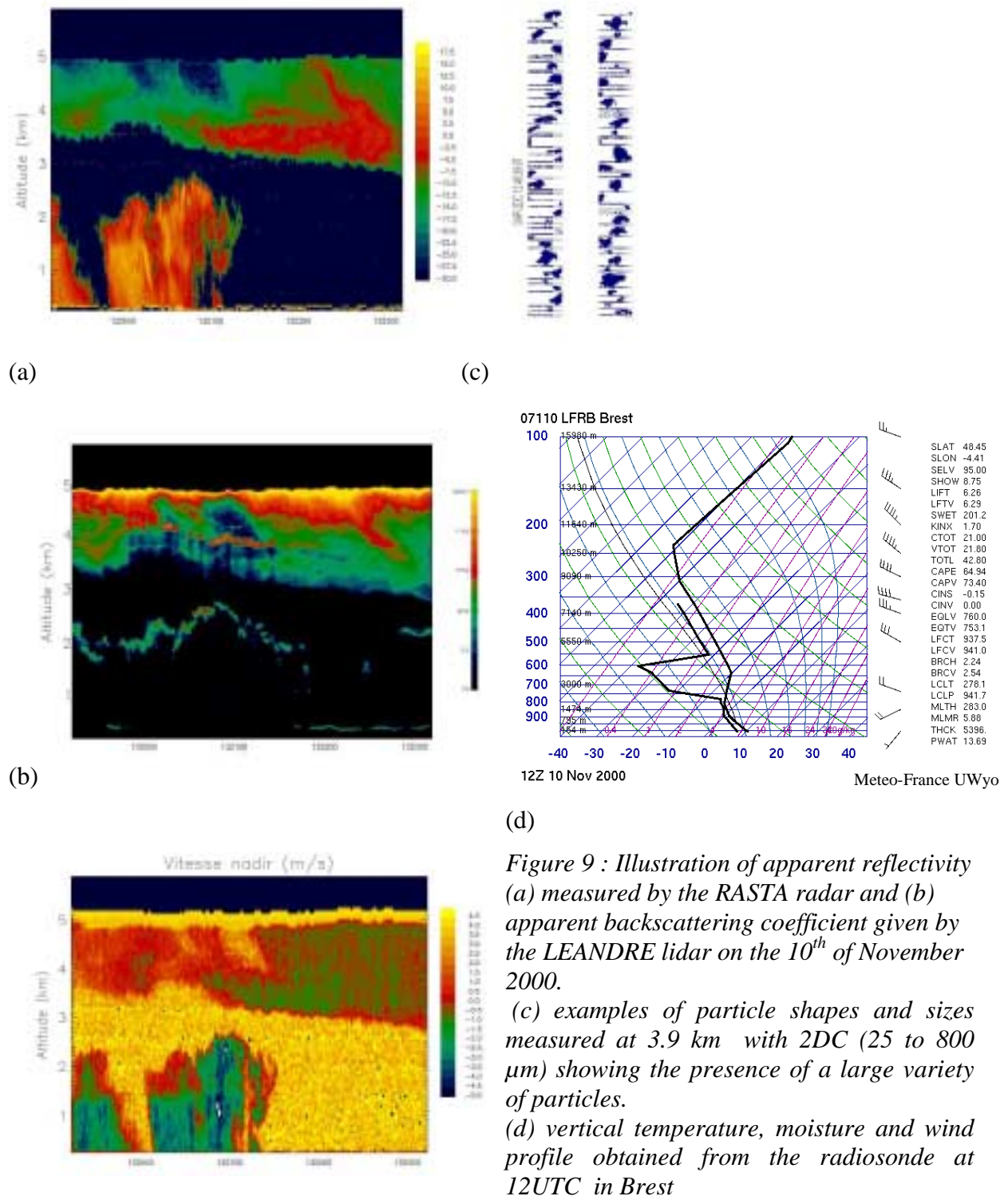


Figure 8 : a) Aladin forecast for the 17 November (analysis at 36 h) b) observations on the 17 November between 8:00 and 20:00 UTC with the ground-based lidar SLIM

### 2.3.4 Airborne measurements : 10 November case study

Figure 9 shows the measurements taken by the airborne radar and lidar on 10 November. The lower cloud layer, which is a precipitating cumulus, is well described by the radar. The backscattered lidar signal only describes the top of this precipitating layer mainly composed of water in its lower part. A good penetration of the lidar and radar beam into the upper cloud layer between 3 and 5 km is observed. This cloud can be identified as an iced altostratus where small and large particles are mixed (Figure 9c).



The temperature profile measured in Brest is given in Figure 9d. It shows the presence of two moist layers. One below 2.5 km and the other above 4 km. It is to be noticed that the sonde measurements were taken before the flights, so that the elevated cloud layer was somewhat higher than observed by the radar and lidar. The zero degree isotherm is observed at 1 km increasing during daytime up to 1.5 km, where a change in reflectivity is seen in Figure 9a to correspond to the transition between ice and water (radar bright band). The structure of right cell of the cumulus layer is more complex due to vertical motions and the bright band is not so clearly observed. In the upper cloud layer, the temperature is varying from  $-8^{\circ}\text{C}$  at 3 km to  $-20^{\circ}\text{C}$  at 5 km. On the spectrum measured in the lower part of the elevated layer (Figure 10), and particle size observed (Figure 9c) both small and large particles are observed. The bimodal distribution observed reflects the presence of small particles with diameters from 10 to 20  $\mu\text{m}$ , which could be water droplets, and large crystals 200  $\mu\text{m}$  in diameter corresponding to aggregates.

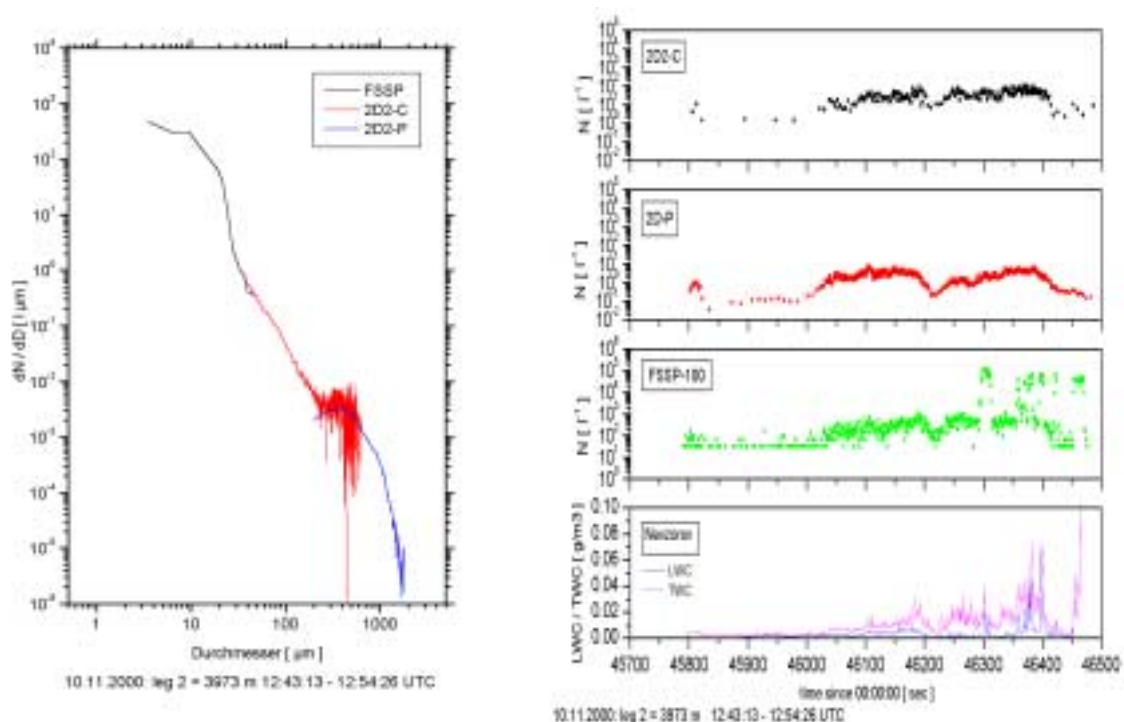


Figure 10 : In situ measurements made by GKSS from the Merlin IV. The size distribution on the left figure shows the large occurrence of particles of small diameter (10-20  $\mu\text{m}$ ) possibly due to water layers as seen from the measured total water and liquid water contents (right figures). Also given on the four diagrams on the right is the concentration of particles for the three probes (increasing size) as a function of time and the total and liquid water content measured at the same time by the Nevzorov. Notice the increase in liquid water related to small particle concentration increase after 46 300 s.

Thin layers with higher backscattering are detected by the lidar at an altitude ranging from 3.9 km to 4.2 km (see Figure 9 b). As this layer is not detected by radar, its composition is most probably small water droplets. The Merlin was flying within the cloud at an altitude of about 4-4.2 km. The presence of water is confirmed by the in situ measurements from the Nevzorov sonde measuring both liquid and total water contents (Figure 10 b) and the TW probe (not shown) and consistent with a low depolarisation observed on the lidar signal. Liquid water

content is reaching  $0.08 \text{ g.m}^{-3}$  in this layer. Turbulence is expected not to be large enough in this stratiform layer to mix water under its different phases.

Microphysical and radiative parameters have been retrieved from the synergetic and analytic radar/lidar algorithms (see annex C for an extensive description of the algorithms).

The synergetic algorithm with segmentation on the size distribution  $N_0^*$  has been done on 8 instrumental gates (about 120 meters). This is why  $N_0^*$  values reported in Fig 10a. seem to be broken up. In this present case effective radii are calculated with the hypothesis of the presence of ice only. Values of the effective radius obtained from the algorithm range from 60 to  $100 \mu\text{m}$  and ice water content are ranging from  $0.001$  to  $0.04 \text{ g.m}^{-3}$  in the altostratus. A different algorithm was applied for the analysis of the super-cooled layer. Since the  $N_0^*$  value is not really different below and above the super-cooled layer, we have used this value and the reflectivity to calculate the ice water content in this layer (from the power law relationship).

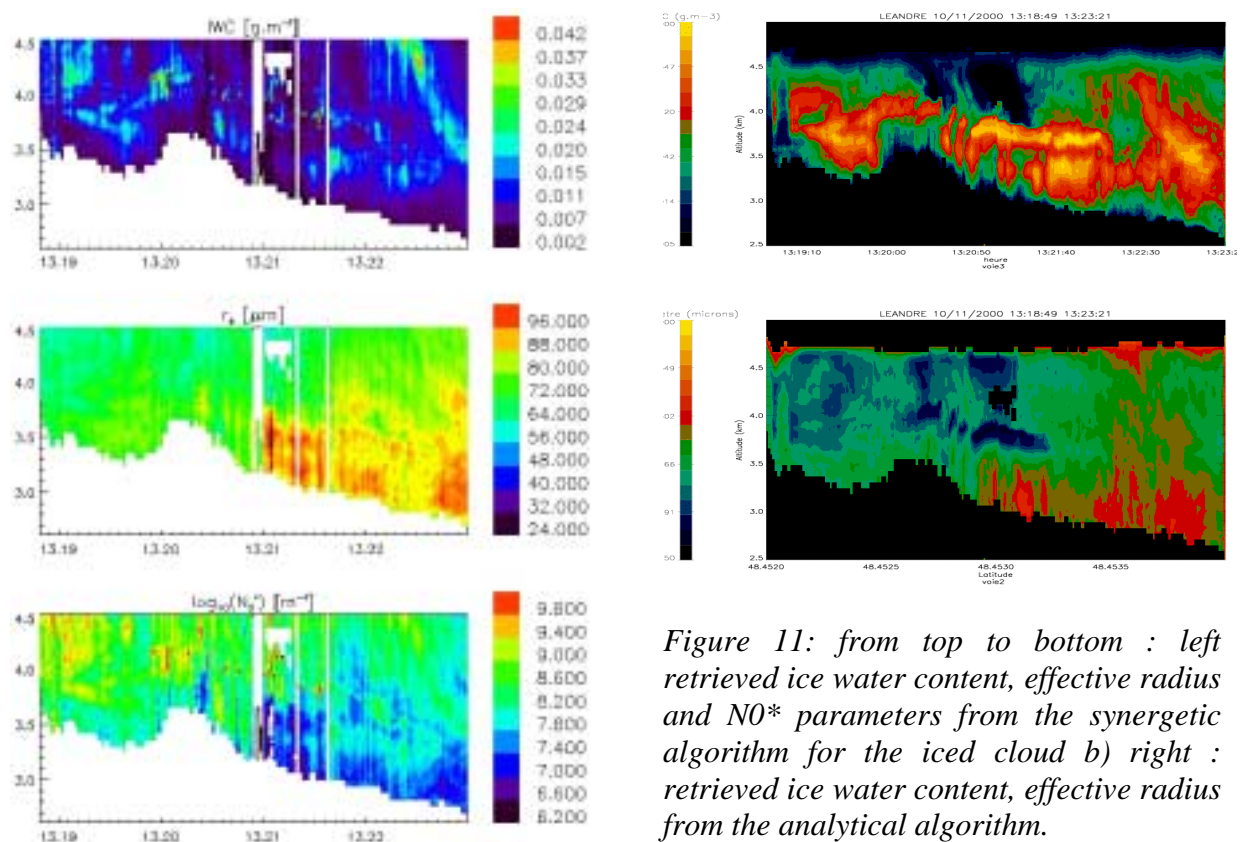


Figure 11: from top to bottom : left retrieved ice water content, effective radius and  $N_0^*$  parameters from the synergetic algorithm for the iced cloud b) right : retrieved ice water content, effective radius from the analytical algorithm.

Since liquid water is mainly seen by the lidar, we have considered an inverse model which only takes into account the lidar measurements and assumes the droplet concentration is constant and corresponds to marine clouds ( $50 \text{ cm}^{-3}$ ). Values between  $2$  and  $6 \mu\text{m}$  are found in the super-cooled layer close to what is expected in such a layer (Francis et al., 1998).

The water content is seen to be low except in the thin super-cooled water layer (up to  $0.06 \text{ g.m}^{-3}$ ) where it reaches values about 5 times larger. This is in good agreement with what has been measured in situ as reported in Figure 10.

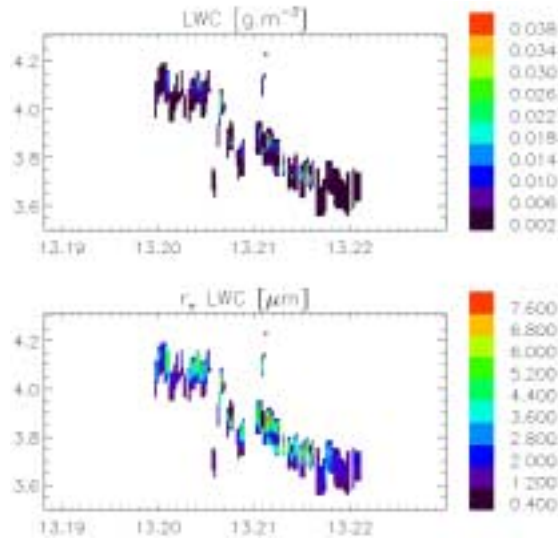


Figure 12 : Liquid water content and effective radius of droplet in the super-cooled water layer as obtained from lidar data analysis.

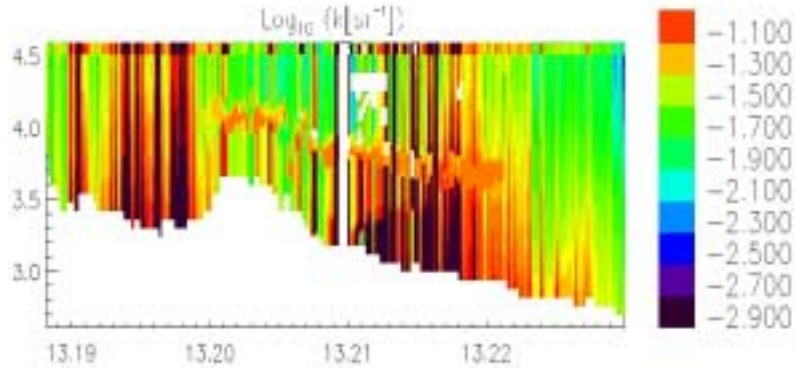


Figure 13 : Cloud phase function at 180° derived from the analysis

In the analytical algorithm the variation of the backscatter-to-extinction ratio is assumed to follow the relationship given by Platt (2002) as a function of temperature for mid-latitude. For lidar measurements, an effective value of  $k$  needs to be considered accounting for the multiple scattering. The value used is such as  $\text{Log}_{10} k$  is about  $-1$ . One can see that the values retrieved by the synergetic algorithm is comparable although slightly smaller.

The overall retrieved diameter is larger than  $120 \mu\text{m}$  except in a few areas or layers where it decreases down to  $60 \mu\text{m}$ . As seen from figure 9, this corresponds to layers where lidar signal is enhanced and radar signal does not show strong variations.

Observations and retrievals are reported in Table 2.

| Parameter           | VAR Z algorithm | Analytical Algorithm | In situ measurements |
|---------------------|-----------------|----------------------|----------------------|
| $D_e (\mu\text{m})$ | 100-170         | 80-200               | 50 – 120             |
| IWC (g.m-3)         | 0.005– 0.02     | 0.01                 | < 0.02               |
| LWC (g.m-3)         | 0.00 – 0.02     | 0.05                 | < 0.08               |

Table 2 : Comparison of values derived from the two algorithms with the in situ measurements

A fairly good agreement is obtained between the values derived from the radar-lidar algorithms and in situ measurements.

### 2.3.5 Cloud dynamics

Among the dynamic properties of clouds two important aspects are addressed here : the retrieval of the along-track horizontal and vertical wind components, and the retrieval of the terminal fall velocity of the hydrometeors  $V_t$ . Knowledge of water drop and ice crystal terminal velocities is indeed particularly important for an adequate representation of particle sedimentation in operational forecast and climate models. Several parametrisations have been proposed in the form of power laws relating terminal velocity and diameter for liquid drops (Rogers, 1976) or for ice clouds (Heymsfield and Iaquinta, 2000) and more recently a unified treatment has been made proposed for all particle types (Khvorostianov and Curry, 2002). The determination of this parameter is of interest to constrain the models and active remote sensing offers this capability (Matrosov and Heymsfield, 2000). The objective is to develop tractable statistical relationships between  $V_t$  and  $IWC / V_t$  and  $r_e$  to be used in models.

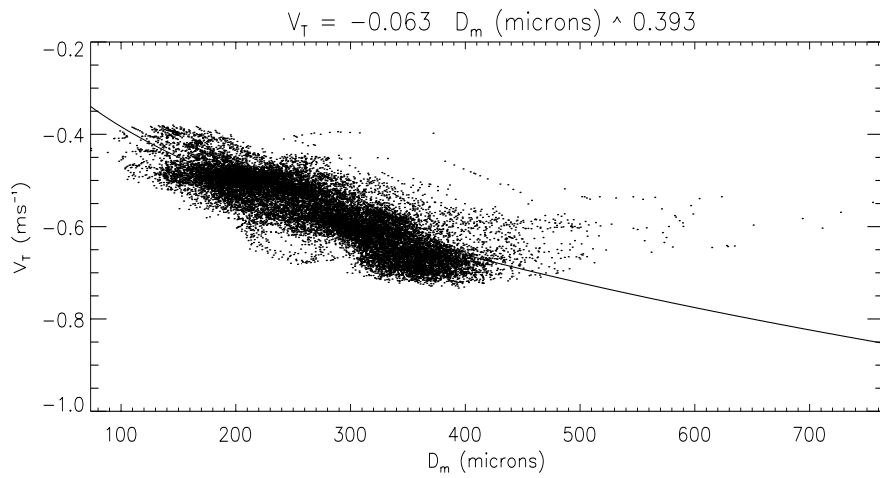
In the case studied, the vertical velocity has been analysed in the cloud as a function of the microphysical properties derived from the combined statistical algorithm. The total vertical speed (air speed  $w$  and particle fall speed  $V_t$ ) is first retrieved from the dual beam measurements. The particle fall speed is then obtained from a relationship between the radar reflectivity and the vertical speed as  $w$  is assumed to average out on a statistical basis (see details in annex D).

The first step of the retrieval is to recover the horizontal particle velocity  $V_{//}$  and the vertical component ( $V_{t+w}$ ) using equations given in annex D. The second step is to use a statistical relationships between ( $V_{t+w}$ ) and the radar reflectivity  $Z$  to further retrieve  $V_t$ . Terminal fall velocity and reflectivity are integral parameters of the particle size distribution (PSD). Ulbrich (1983) for a Gamma-type PSD, and Testud et al. (2001) for a normalized PSD, established that the relationships between integral parameters were represented by power-law relationships. The method proposed here consists of estimating statistical power-law relationships  $V_t = a Z^b$  between terminal fall speed and radar reflectivity by fitting the individual estimates of ( $V_{t+w}$ ) and  $Z$ , with caution exercised in order to process a time span long enough to make the mean vertical air velocity vanish with respect to the mean  $V_t$ .

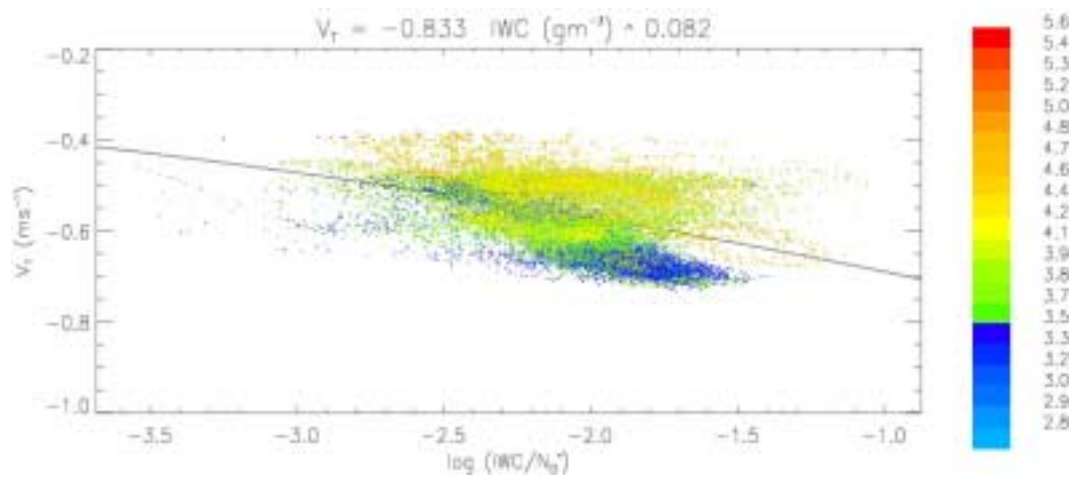
The statistical relationship between  $V_t$  and  $Z$  has been derived from the dual-beam Doppler observations of the cloud radar, and the radar reflectivity has been translated into terminal fall velocity in the 2D vertical cross-section. Values of  $V_t$  ranging from  $-0.9$  to  $-0.4 \text{ ms}^{-1}$  are retrieved within the cloud. It is to be noted that rimed crystals (crystals with droplets) as expected here have been observed to fall at a speed about twice larger than drier ones ( $0.5 \text{ m/s}$ ) Then, using these results,  $V_t$  can be plotted against the mean melted diameter  $D_m$  (Fig. 14a) and  $IWC$  (Fig. 14b) in order to develop statistical relationships between these quantities for this altocumulus case. The obtained exponent coefficient of the dependence with diameter is about 0.3-0.4, which is comparable to what is expected (Rogers and Yau, 1996; Khvorostianov and Curry, 2002).

It is seen though in Fig. 14 that some problems still need to be addressed. Indeed, there is a lot of scatter around the fitted curves, although a satisfying general trend is observed. This is attributed to the fact that particles have different shapes and sizes and moreover that this

altostratus includes super-cooled water droplets (see Figure 10 in situ measurements and in Figure 9 a distinct layer about 200m thick is observed on the lidar backscatter coefficient and depolarisation ratio (not shown)).



a)



b)

Figure 14 : vertical speed of particles deduced from dual beam radar measurements as a function of the (a) median diameter et (b) normalized ice water content.

Comparing Figure 14 a and b, one can see that when the altitude is considered as an additional constraint the dispersion can be reduced and different dependence can be evidenced. These differences are induced by the size of the particles. Upper altitude crystals are falling at a smaller speed, whereas lower ones having a larger size and possibly being wetter are falling at a larger speed.

This type of (preliminary) relationships are readily useful to large-scale models, since generally  $V_T$  is diagnosed from the particle size or  $IWC$ .

### 3- PART 2 : THE BRETIGNY CAMPAIGN

The second phase of CLARE 2000 was held in Brétigny-sur-Orge, France. It was aimed at complementing the first phase with airborne radar and lidar observations. Two aircraft were involved in order to document the microphysical, radiative and dynamic properties of clouds : the ARAT aircraft, carrying the RASTA cloud radar and the LEANDRE I backscatter lidar, and the Météo-France MERLIN-IV aircraft carrying in-situ microphysical sensors for in-situ validation. Owing to the maximum flight level of the ARAT (5.5 km), the priority meteorological targets were mixed-phase or ice midlevel clouds and stratocumulus. Four flights were made with the two aircraft flying above and in these clouds. A description of the flights and general results will be given here. Analyses similar to those performed for phase 1 are under way, and we will here focus more on relationships between in situ microphysical parameters (IWC) and remote sensing measurements, such as those used for phase 1 in the combined algorithm (see annex C). Cloud dynamics is analysed in a nimbostratus case.

#### 3.1 Meteorological situation

9/03/2001 case: altostratus and altocumulus multilayer clouds.

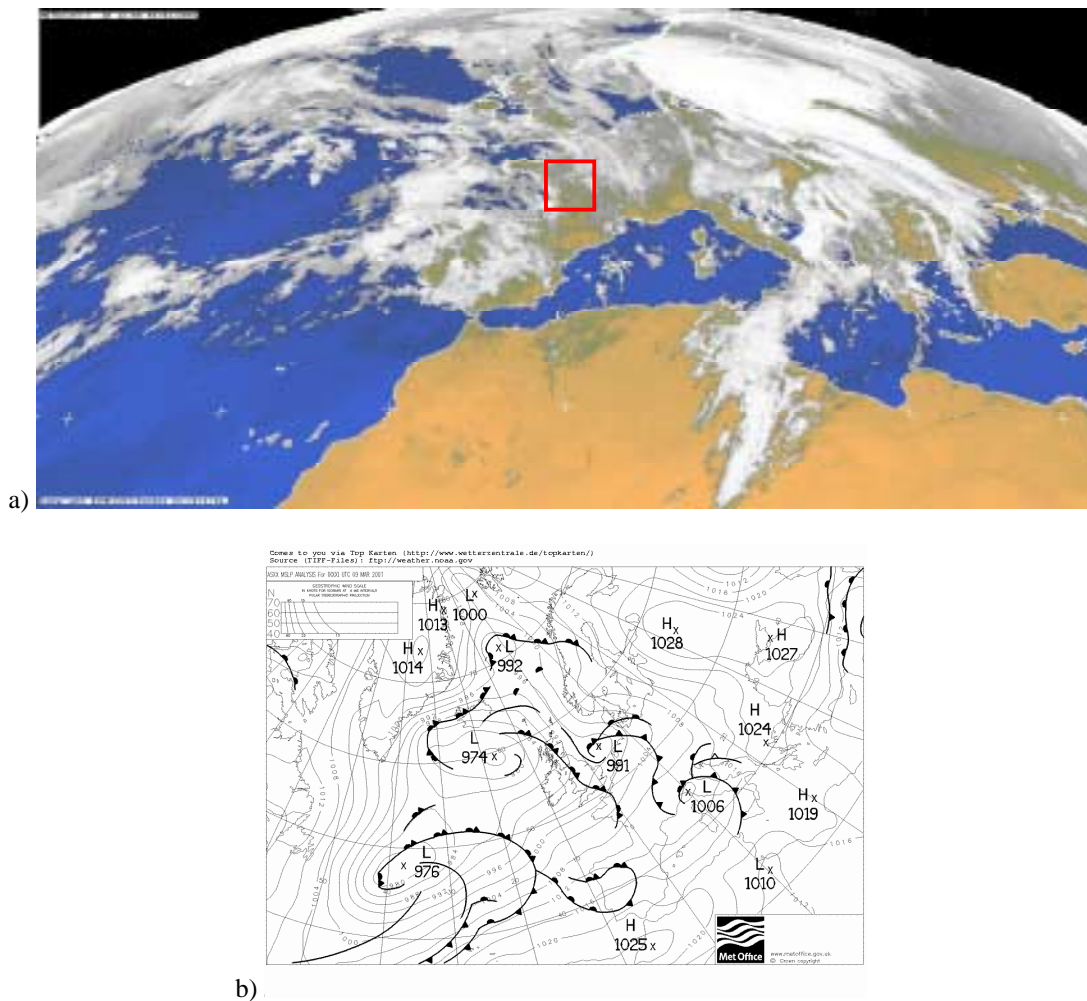


Figure 15 a) Meteosat image for 9 March 2001 at 12:00 UTC provided by Eumetsat and b) corresponding surface analysis made at UKMO for 00 UTC. The squared area shows the measurement area

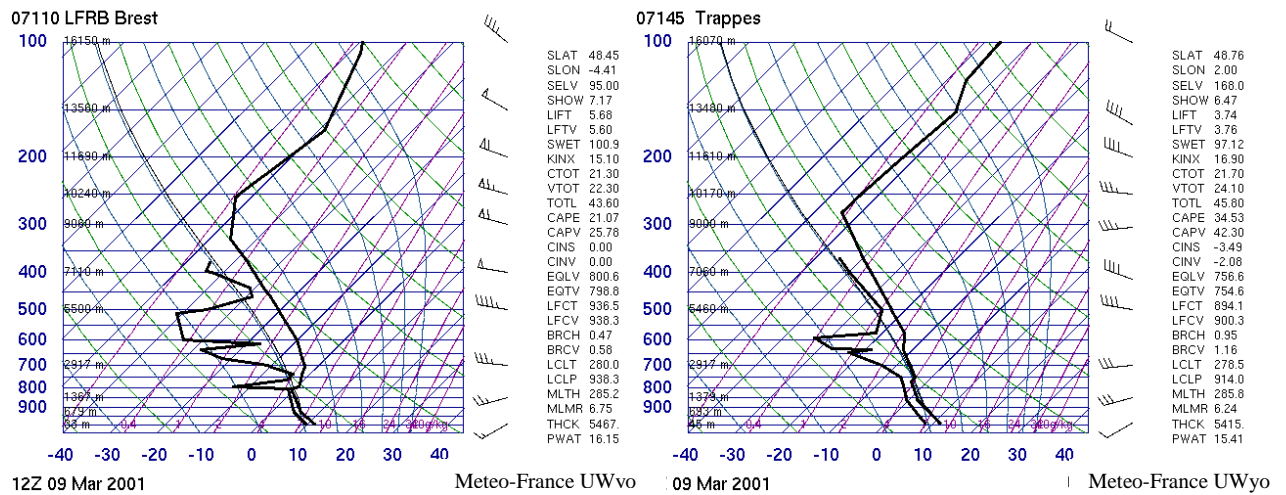


Figure 16 : soundings performed in Brest and Trappes

Measurements were taken in the Orleans area, south of Brittany along the two main tracks which direction NE-SW allowed to sample the frontal clouds. The vertical structure is showing the presence of two main cloud layers, the lower one extending up to 3 km. The remote sensing aircraft was flying below the upper level cloud at 5.5 km.

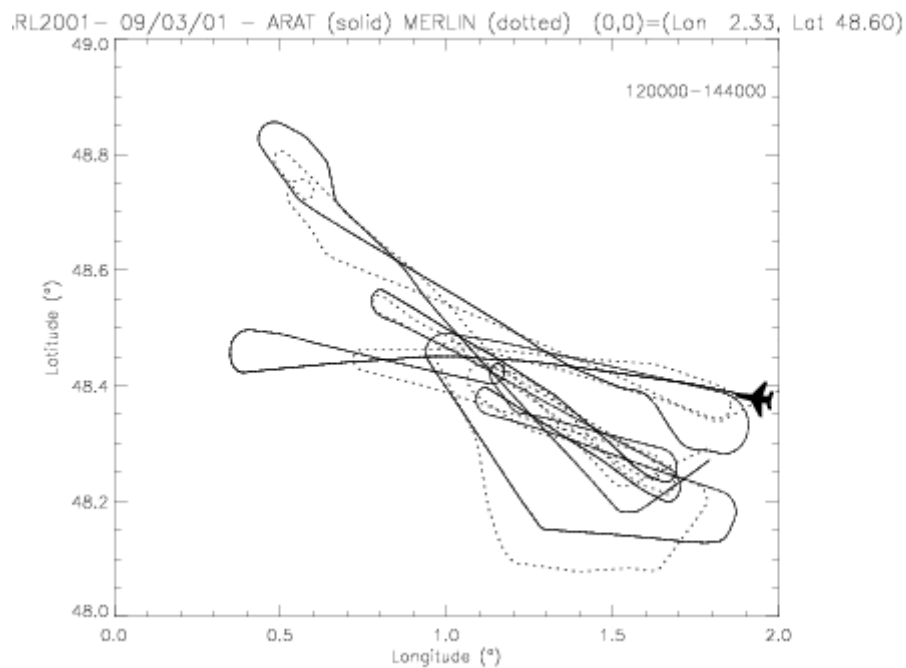


Figure 17 : Flight track of the ARAT and Merlin on 9 March 2001

12/03/2001 case: iced precipitating levels of a cumulus congestus cloud field.

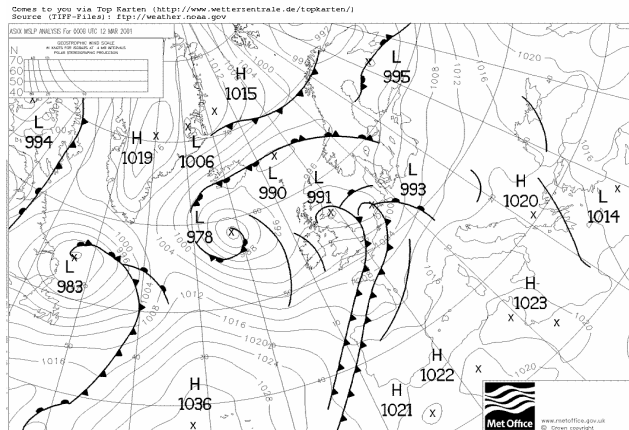


Figure 18 a) Meteosat image for 12 March 2001 at 12:00 UTC provided by Eumetsat and b) corresponding surface analysis made at UKMO for 00 UTC. The squared area shows the measurement area.

Measurements were taken close to the cold front, as it passed over France (see Figures 18 and 19) over developing Cu.

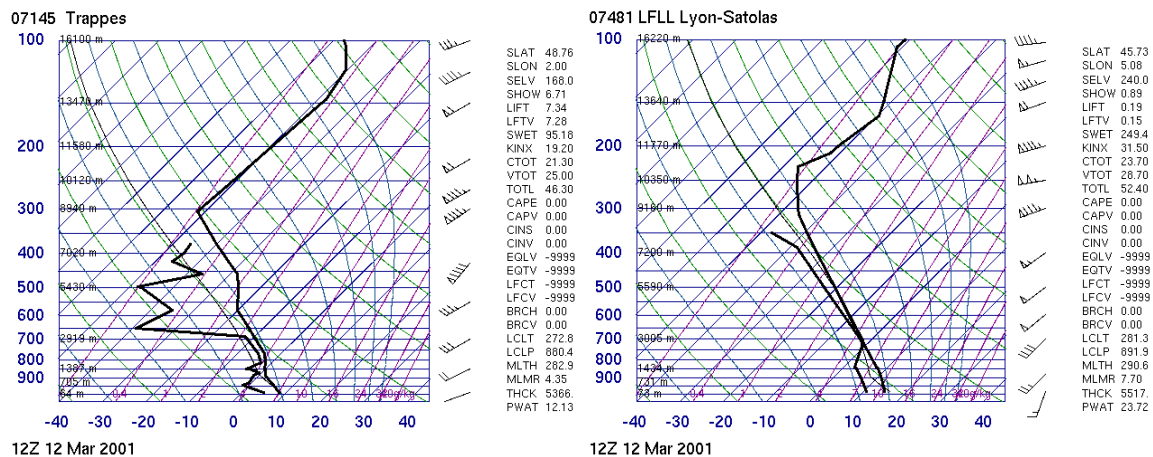
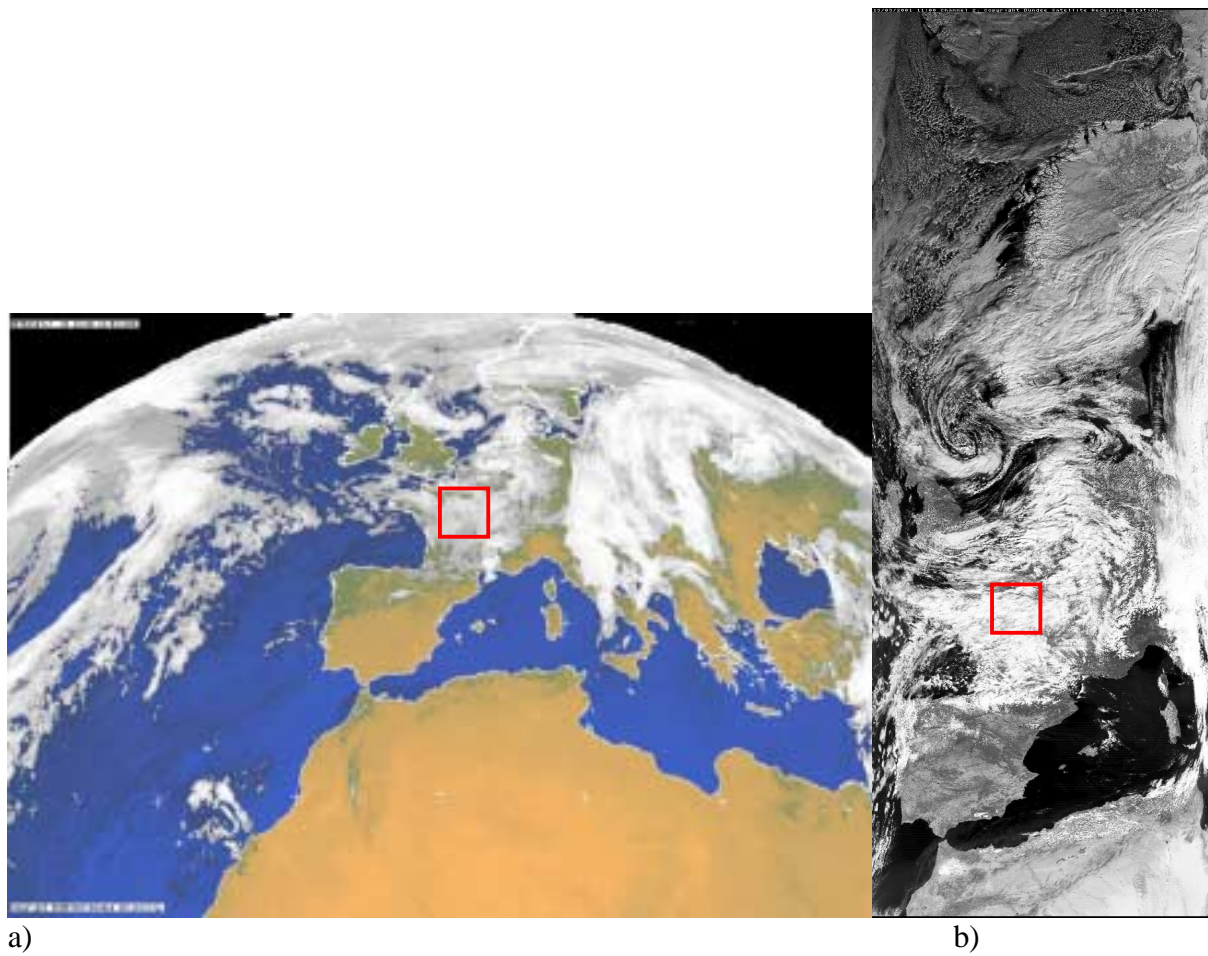


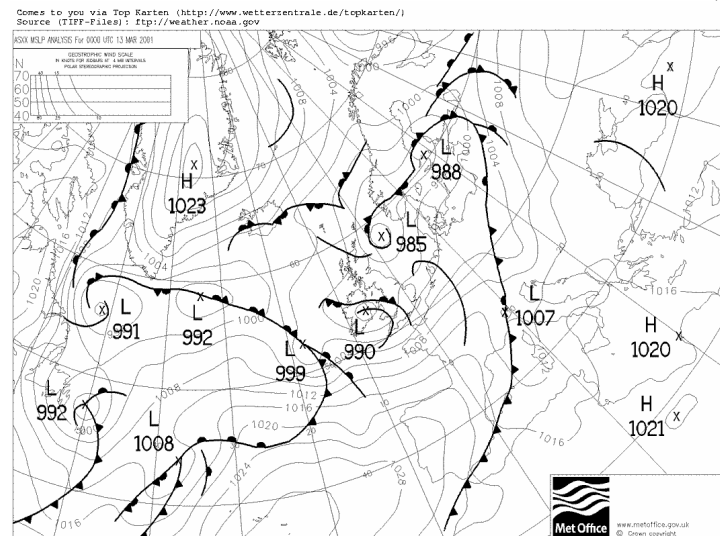
Figure 19 : soundings performed in Brest and Trappes

13/03/2001 case: iced precipitating levels of a nimbostratus cloud (warm front situation).



a)

b)



c)

Figure 20 a) Meteosat image for 13 March 2001 at 12:00 UTC provided by Eumetsat b) MODIS image in visible channel (NASA) and c) corresponding surface analysis made at UKMO at 00 UTC. The squared area shows the measurement area

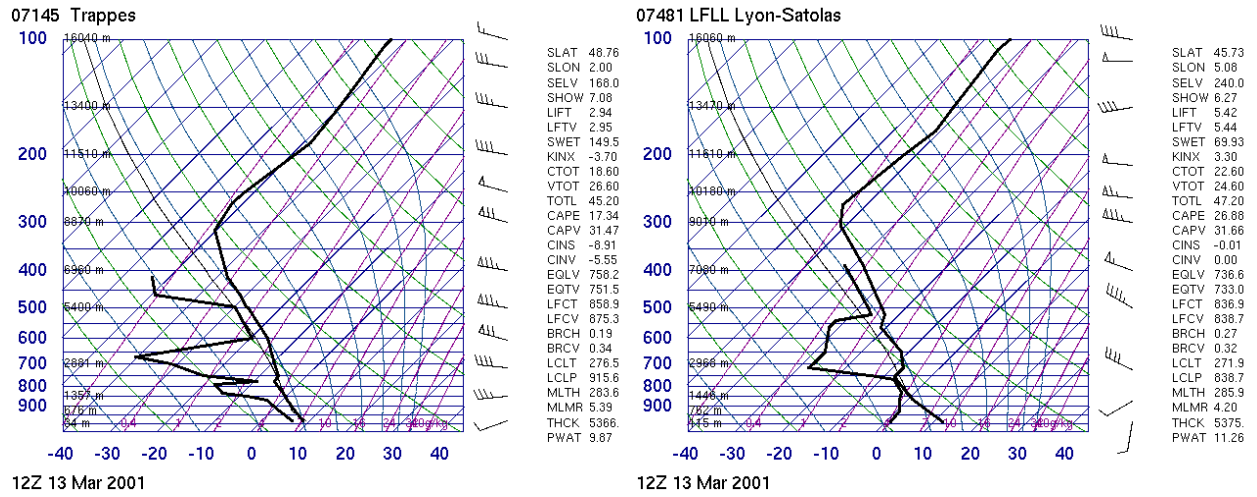


Figure 21 : soundings performed in Brest and Trappes

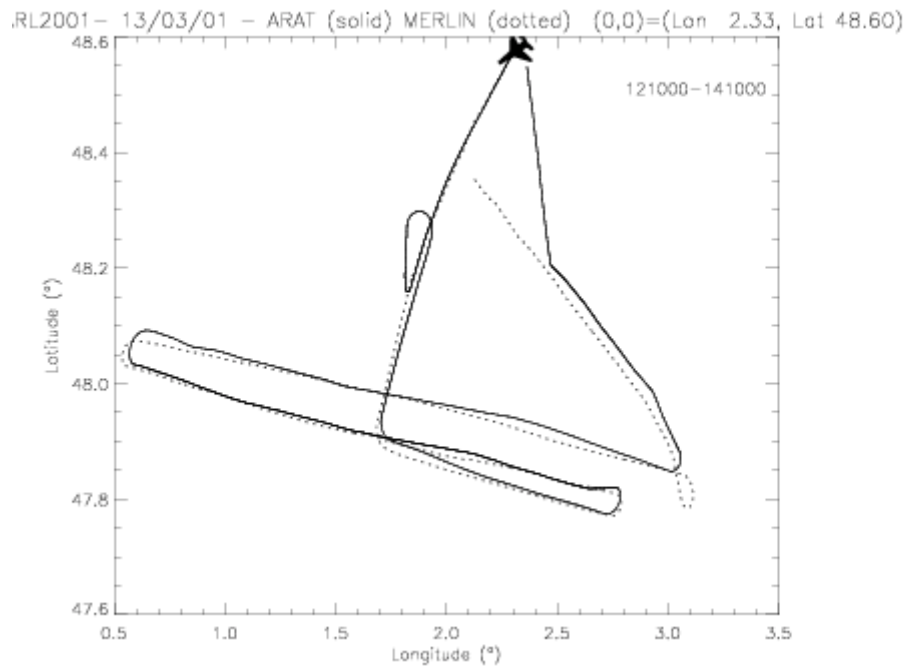


Figure 22 : Flight track of the ARAT and Merlin on 9 March 2001

16/03/2001 case: alto stratus iced layer and after in a small cumulus cloud field layer.

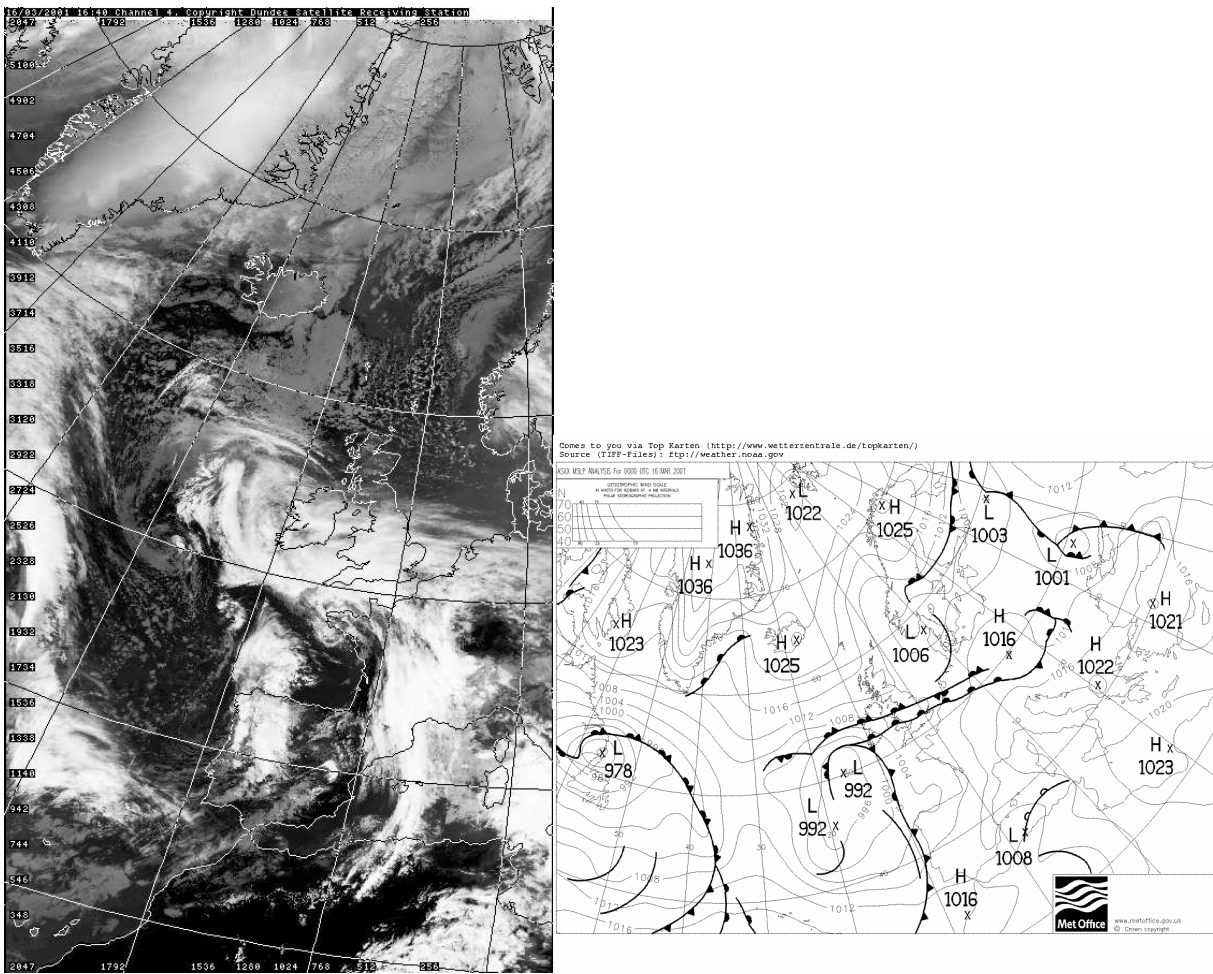


Figure 23 a) AHRH image over Europe on 16 March 2001 at 16:40 UTC in the IR channel and b) corresponding surface analysis made at UKMO for 00 UTC. The squared area shows the measurement area

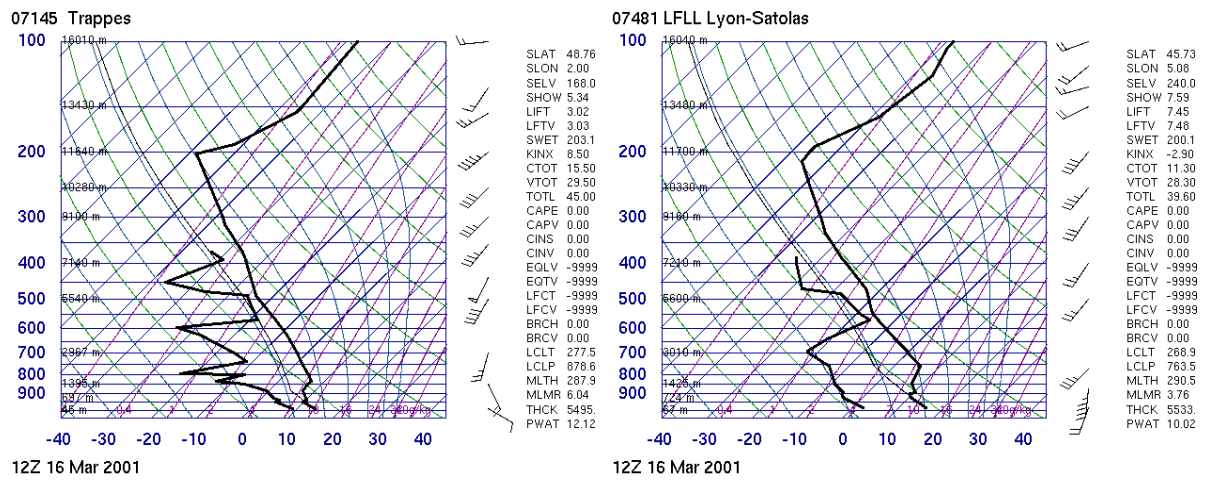


Figure 24 : soundings performed in Brest and Lyon

## 3.2 Measurements performed

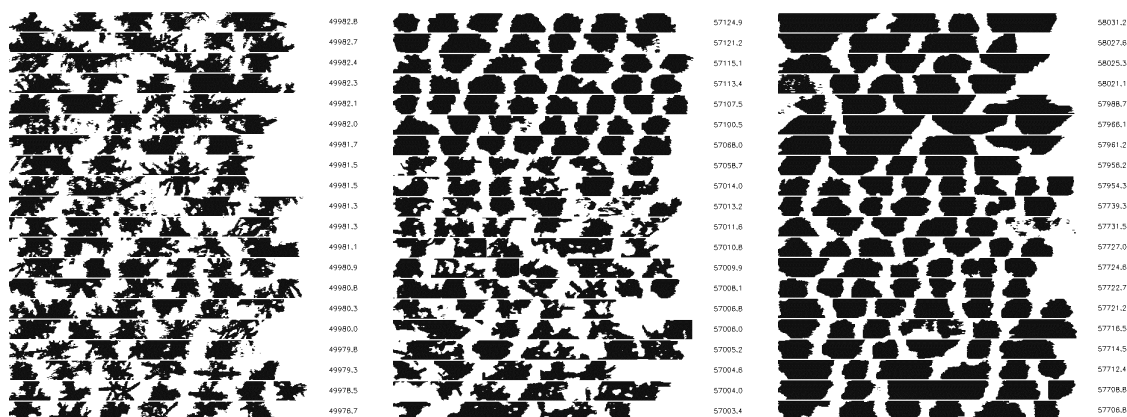
During the march 2001 phase of the RALI experiment, four coordinated flights was performed using the two aircraft in various frontal meteorological situations.

| Date     | ARAT<br>Radar/<br>Lidar | MERLIN | Cloud type  | Comments  |
|----------|-------------------------|--------|---|---|
| 09.03.01 | XX                      | X      | Alto-stratus and alto-cumulus multilayer clouds.      | At the in-situ measurements aircraft level the concentration of precipitating particles is low (yielding to maximal reflectivity less than 0 DbZ). Super-cooled water in the upper level altostratus.           |
| 12.03.01 | XX                      | X      | cumulus congestus cloud field                         | Precipitating ice. A large variability of crystal shapes are observed during the coordinated legs, from low density snowflakes to highly rimed graupels.  |
| 13.03.01 | XX                      | X      | nimbostratus cloud (warm front situation)             | Ice precipitating in the cloud. During all the coordinated legs, the crystal shapes have low variability and are mainly represented by agglomerates of columns or dendritic crystals (low density snow flakes). |
| 16.03.01 | XX                      | X      | alto stratus iced layer and small cumulus cloud field | During this flight, high resolution measurements of temperature are available with a sonic thermometer probe.   |

## 3.3 Data Analysis

### 3.3.1 In situ Data analysis

In situ measurements from the MERLIN aircraft were made for all the legs of the experiments. Examples of data are reported in Figure 25 for the 12 March 2001.



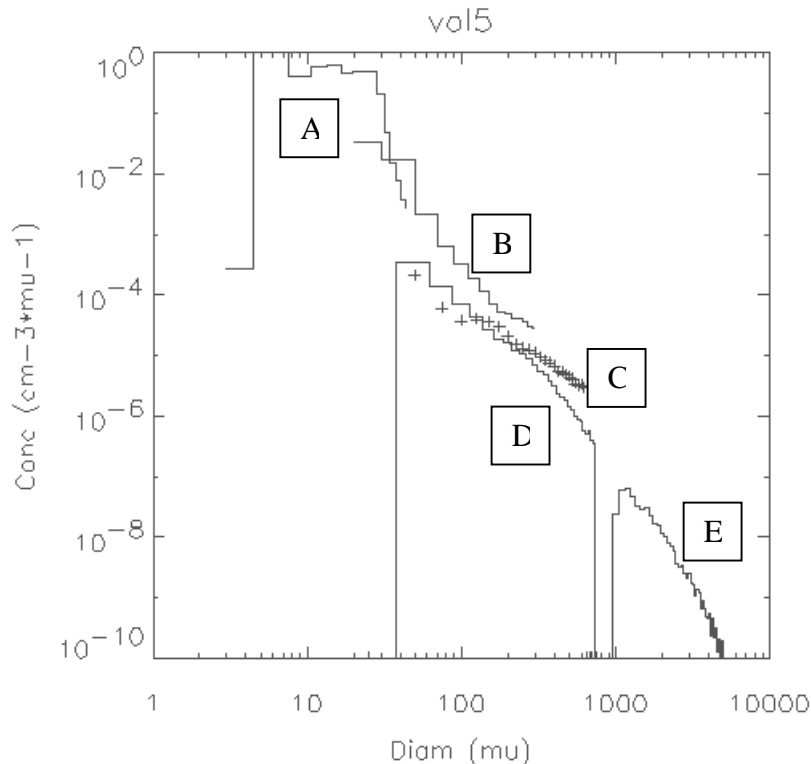


Figure 25 : On the top, example of 2DC image sampled during a transition between a low density snowflakes region and a high density graupel region during the 12/03/2001 (Cu.Cg) case. Bottom : the mean size spectrum for the coordinated legs of this flight.

The spectrum reported in Figure 25 is obtained with different probes and with use of different definitions of the diameter of the particles. From left to right;

- A : FSSP probe spectrum using spherical assumption and forward diffusion measurement of diameter
- B : CDP probe spectrum using geometrical maximum dimension perpendicular to aircraft trajectory
- C : 2DC spectrum (+) using the same rule than the CDP probe (using only the complete images).
- D : 2DC spectrum using the squared surface of the image to estimate the diameter (using only the complete images)
- E : 2DC spectrum for the image larger than 800 micrometers estimated with the maximal dimension parallel to the flight direction.

All the spectra (and a composite spectra from 50 to 5000 micrometers with 50 micrometers binsize) are available for the four flights with a 1 Hz resolution but the large diameters (important for the estimation of the precipitating rate or the radar reflectivity) have a poor statistical validity at this scale. For the presented comparisons we use a 1 kilometre space scale also compatible with the co-localisation of measurements of the two aircraft.

All the data are available on the LaMp web site ([WWWOBS@univ-bpclermont.fr](mailto:WWWOBS@univ-bpclermont.fr))

The absolute positions of the two aircraft during one experimental leg have been analysed. The trajectories are similar with a 1 km incertitude.

We first test the comparison using the time reference (i.e. compare the two aircraft measurements at the same time). After a look on the relative positions we have used the

geographical proximity (along selected legs) to compare the measurements from the two aircraft (i.e. measurements sampled at the nearest positions). This technique increases the space/time correlation between the measurements of the two aircraft. Note that the ratio between the aircraft velocities and the horizontal cloud structures velocities is large enough (around 10) to allow this “frozen atmosphere” comparison technique.

### 3.3 Data Analysis

A first analysis of the data gathered during this second phase, was performed to compare size particle and radar reflectivity. In order to derive microphysical parameters from in situ data measurements of the size of particles in terms of area or length, a mass-dimension function of the form  $M=A.D^B$  to be assumed. Size is determined from in situ using a geometrical model referring to the dimension of the particles mostly observed. Several geometrical models can be assumed corresponding to different values of A and B coefficients (see Locatelli and Hobbs, 1974 for example). As the size is estimated for compact particles, the ice density is taken equal to 1 g.m<sup>-3</sup>, but this also corresponds to a variable density when the diameter is defined as the one of a sphere of equivalent mass (see Brown and Francis, 1995). We considered D to be the maximal length of the crystals and integer values of B varying between 1 (columns, needles) and 3 for quasi spherical object (graupels) with defined density (see Rogers and Yau, 1996). We then assume the radar reflectivity to be proportional to the square of the ice mass. Note that the high variability of crystal shapes in the convective situations imply a spatial variability for the B exponent. We try now to develop this kind of method using the local measure of the “rugosity” of the crystal images. For example, during the first 100 seconds of the leg 3 (bottom and left on the figure), the in-situ underestimate the radar reflectivity because it is a region of graupels, yielding larger B values (and a larger prefactor A).

We then compare the measured reflectivity to the reflectivity calculated from the particle mass (with  $Z \sim M^2$ ).

#### 3.3.1- 12 March Case

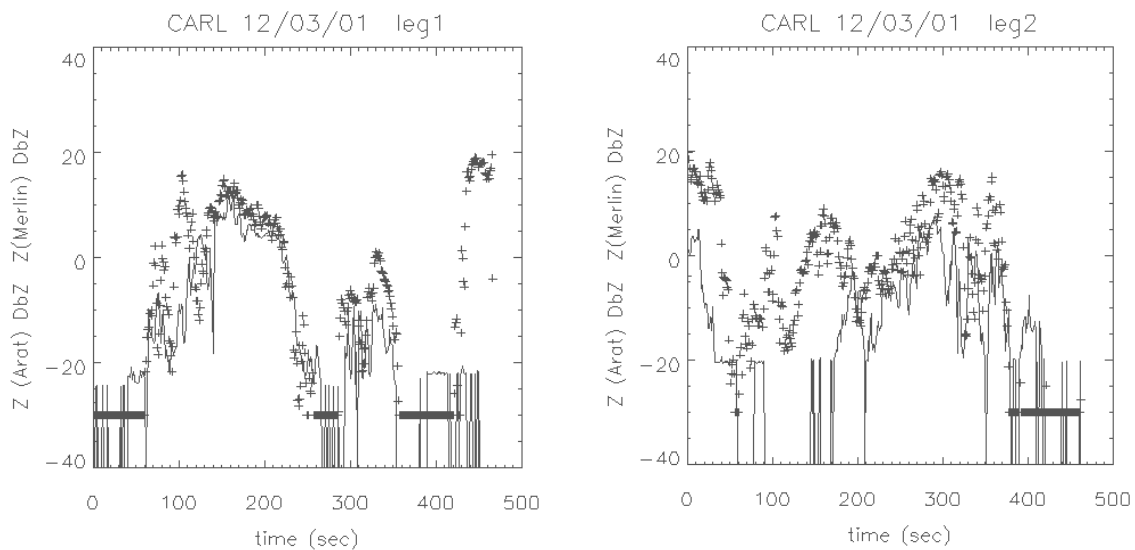


Figure 26 : Comparison of measured (solid line) and calculated (+ symbols) radar reflectivities for the 12 March Case a) for leg 1, b) for leg 2

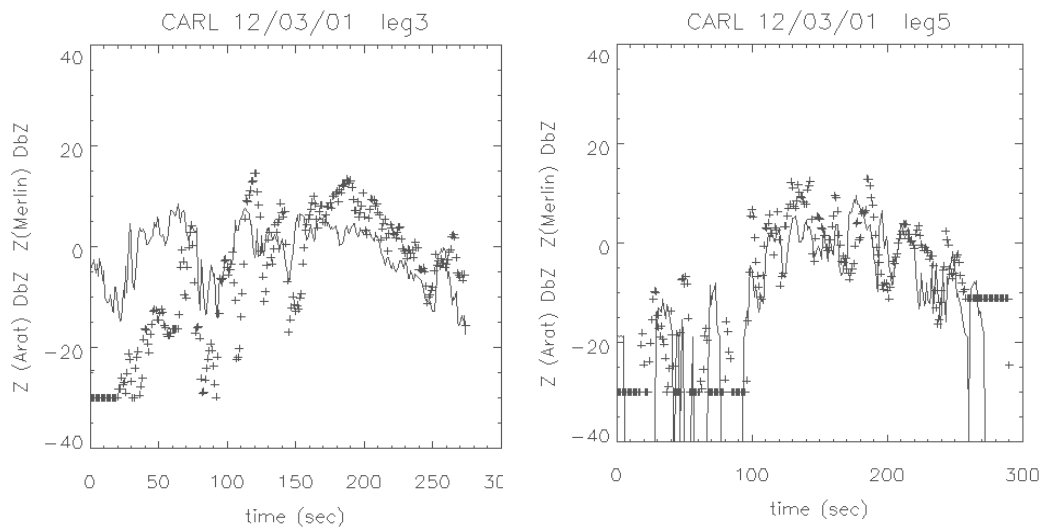


Figure 27 : Comparison of measured (full line) and calculated (+ symbols) radar reflectivities for the 12 March Case c) for leg 3, d) for leg 5

In this flight particles were sampled in Cu-Cg. The remote sensing radar in continuous line and in situ estimations with (+) symbol) for the four legs given in Figure 27.

For this case we use the “in-between” model for  $B=2$  (close to those corresponding to densely rimed radiating assemblage of dendrites  $-2.1-$  or aggregates of same particles or other assemblages  $-1.9-$ , Locatelli and Hobbs, 1974; Rogers and Yau, 1996) gives a better estimate of the in situ reflectivity. The agreement is rather fair on a statistical basis. Some difference is observed at beginning of leg 3. As presented above, this flight shown particle shape ranging from agglomerates of columns to a quasi spherical rimed graupel shape in good agreement with what was found from the comparisons.

### 3.3.2 13 March Case

#### A- Reflectivity-to-microphysics comparisons

On this case, and for three different legs in the nimbostratus cloud (13/03/01), we have compared the nadir reflectivity of the ARAT radar and in situ measurements using the same technique. The flight altitude of the in situ aircraft MERLIN is between 3 and 4 km, about 1 km below the ARAT. The presence of a bright band ( $0^{\circ}\text{C}$  level) characteristic of a nimbostratus layer.

On the figures, the radar reflectivities are plotted with a continuous line, and in dashed line, the estimation of reflectivities is reported using the in-situ observed dimensional spectra and the assumption of a geometrical model of the observed ice precipitation particle shapes. In this case we use a model of agglomerates of columns ( $B=1$ ), in agreement with the observed shapes of the ice hydrometeors. The plot of the reflectivity calculated from in situ measurements is shifted of  $+20$  dBZ for visibility on the figures. The better quantitative agreement between the two reflectivities is obtained with a model of aggregate of four

columns with 100 micrometers basal face fixed size and a maximal length equal to the observed diameter of the image.  
 One can see that the agreement is fairly good over all the legs analysed.

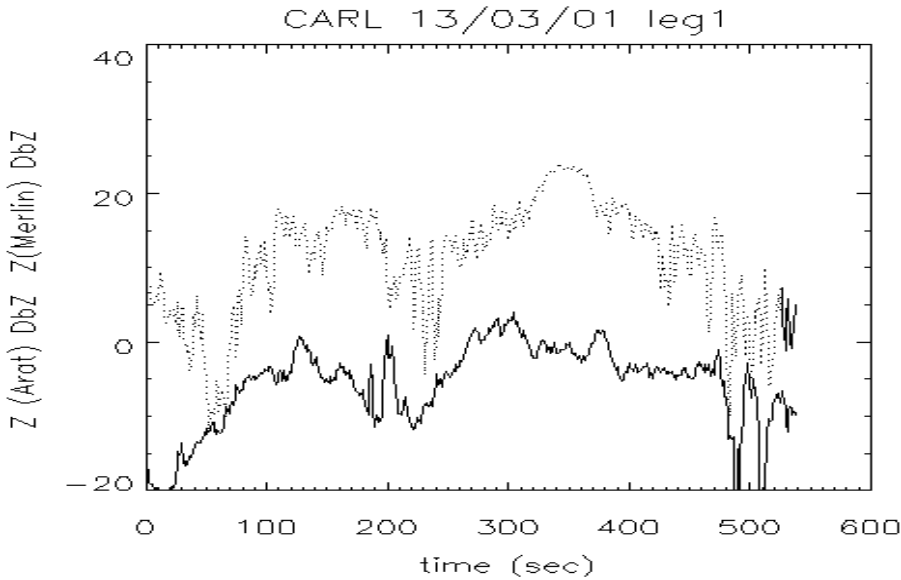
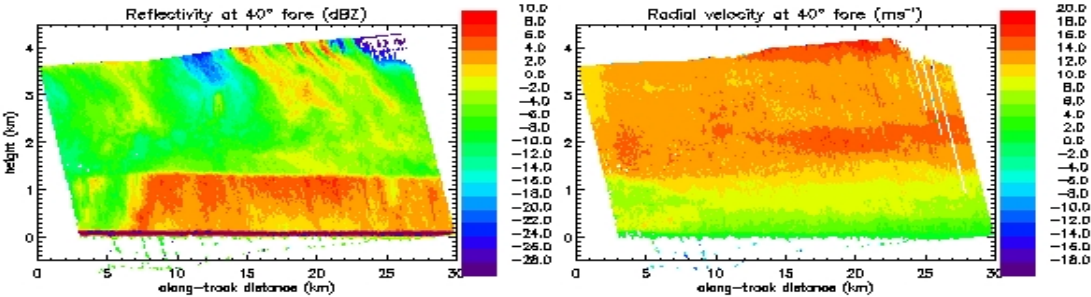
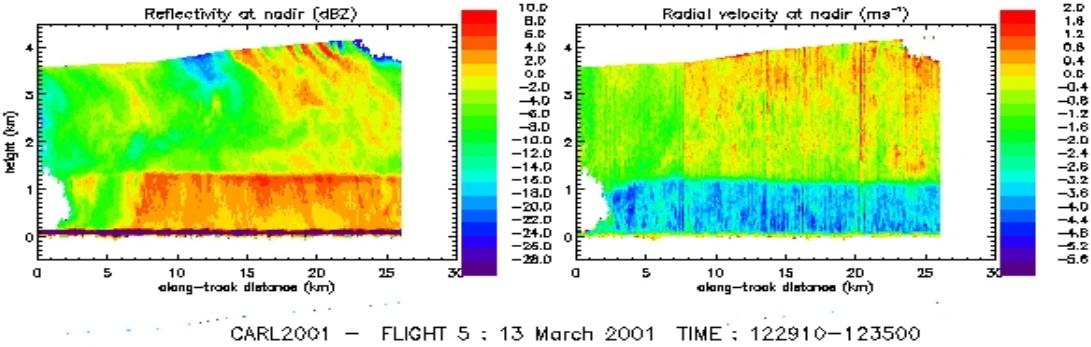
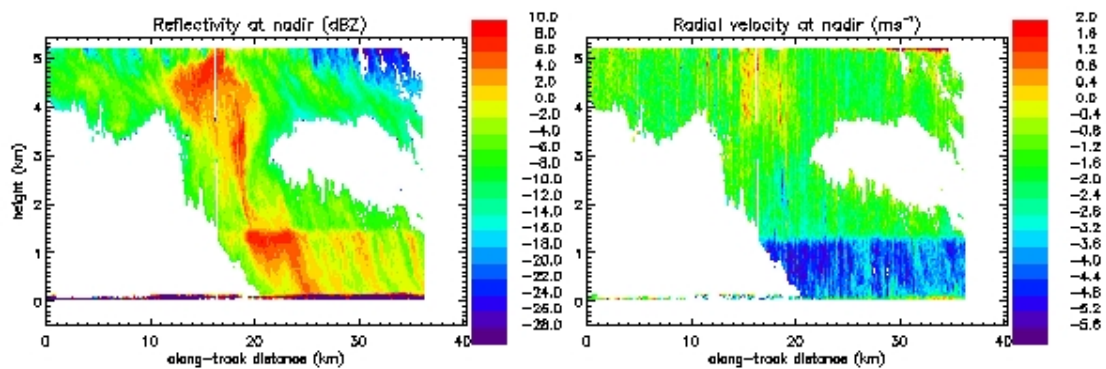


Figure 28 : a) Radar reflectivity and velocity measurements and b) comparison between measured radar reflectivity (solid line) and reflectivity calculated from in situ measurements (dotted line) for leg 1 on 13 March 2001. The calculated reflectivity is shifted of +20 dBZ.



CARL2001 - FLIGHT 5 : 13 March 2001 TIME : 130731-131600

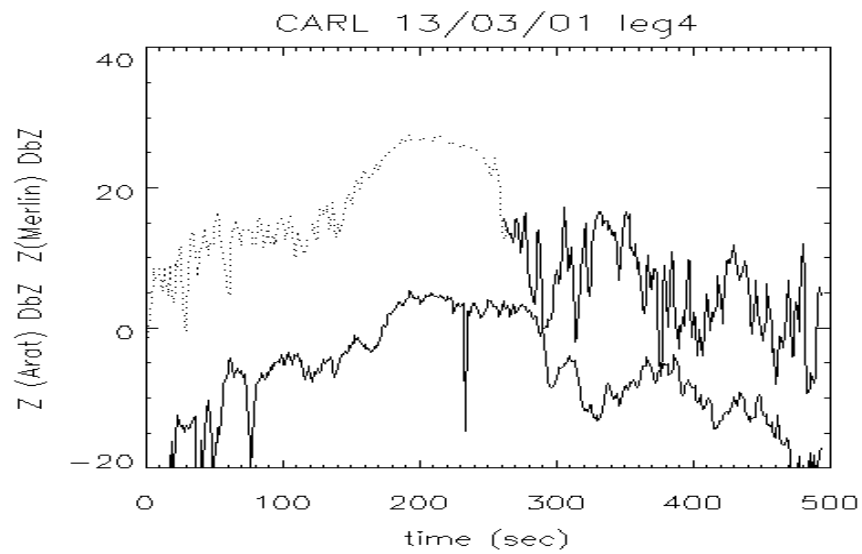
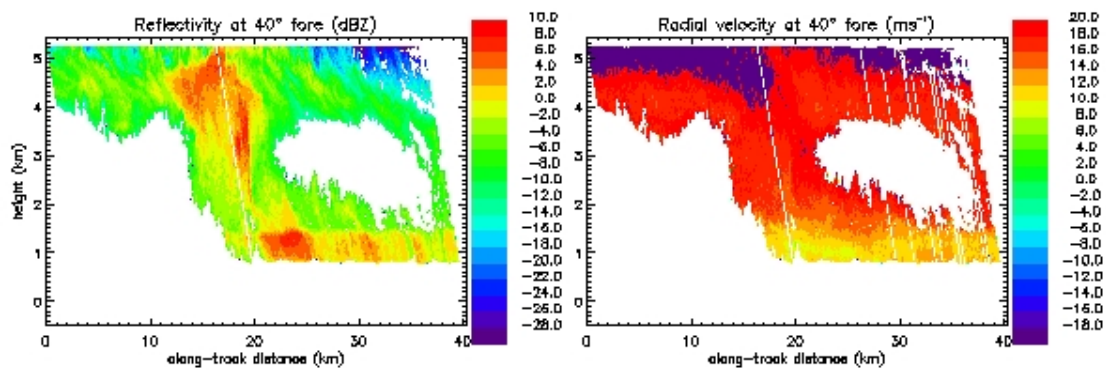
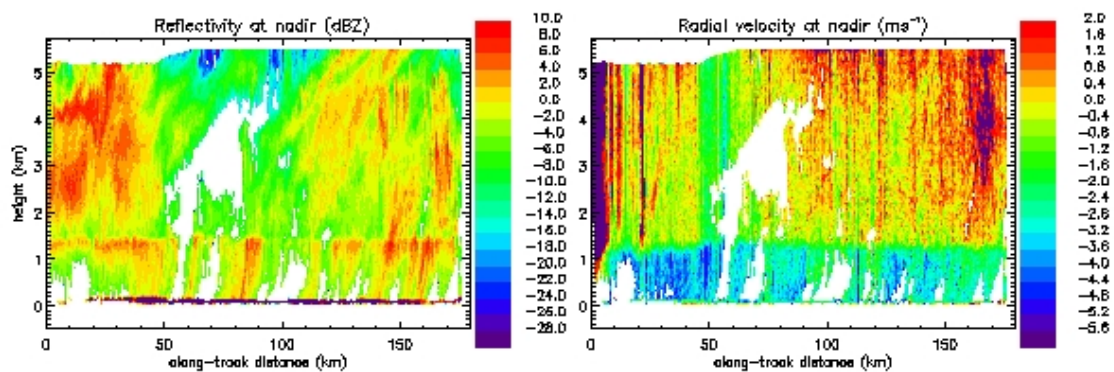


Figure 29 : Same as Figure 28 for leg 4 of 13 March 2001



CARL2001 - FLIGHT 5 : 13 March 2001 TIME : 132700-134759

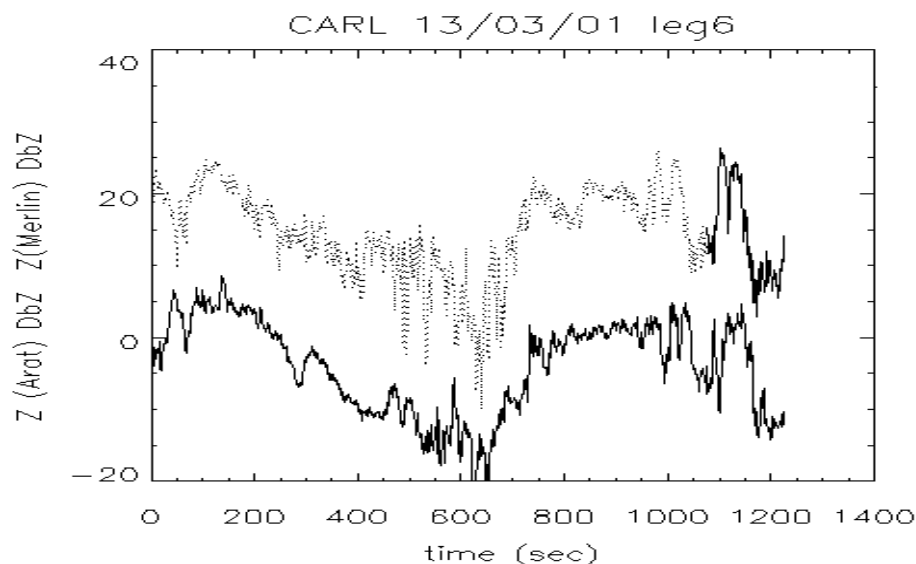
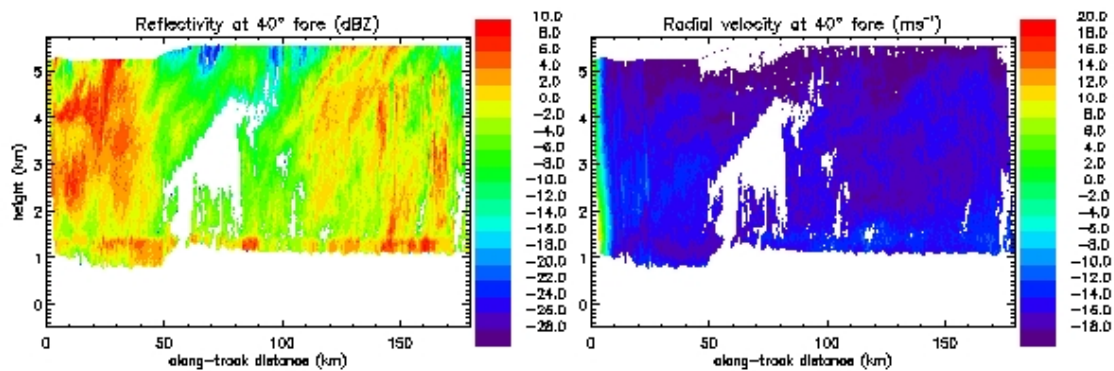
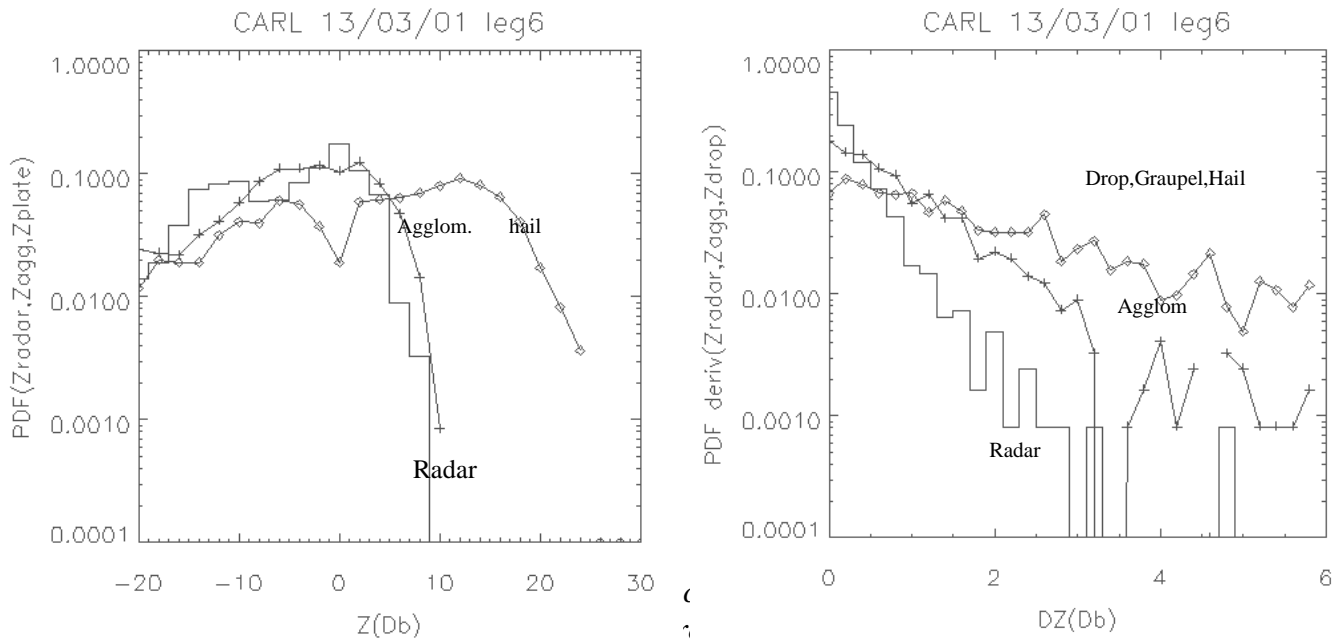


Figure 30 : Same as Figure 28 for leg 6 of 13 March 2001.

## B-Statistical comparisons

Besides the case studies of each legs we compared the probability density function (PDF) of the radar reflectivity and the reflectivity calculated from in situ measurements using different simple geometrical models of hydrometeor shape.



*Figure 31 : a) Measured and calculated radar reflectivity distribution for all legs of 13 March 2001 using two assumptions of shapes (Plates with  $B=2$  and agglomerates with  $B=1$ ) and b) same for the point to point variation in reflectivity*

On the left is given the PDF of the reflectivity for the six legs of the 13/03/2001 nimbostratus case.

The best agreement between the remote measured reflectivity and the observed one occurs for the “agglomerate of columns” geometrical model of hydrometeor shape. The plate model and moreover the drop model (not shown) overestimate the radar PDF width. Note the main result of these figure concern the “shape” of PDF but not the absolute value of the PDF (mainly determined by the prefactor  $A$  of the mass-dimension function) as PDFs were scaled to adjust. In this case it appear that the low  $B$  exponent ( $B=1$ ), characteristic of columns shape give a better qualitative agreement for the radar and in-situ PDF of measured reflectivities.

On the right, the PDF of the increments of the reflectivity measured at 1 Km scale. These PDF are highly non gaussian (and even decrease more slowly than an exponential) indicating a high intermittency of the reflectivity signal. Quantitative comparisons of these PDF are very sensitive to the exact averaging operation performed by the probe used (1D for in-situ and 2D for remote sensing).

## C- Retrieval of dynamical properties

The same method as described before for the Brest phase has been applied to the radar data for the BRETIGNY campaign. The best case of 13<sup>th</sup> March has been selected.

The method proposed before which extracts statistical relationships between  $Vt$  and radar reflectivity  $Z$  has been applied to the dual-beam Doppler measurements of the RASTA cloud radar in the nimbostratus case sampled on March, 13, 2001 in the Bretigny area.

Among the observed cases, the 13 March nimbostratus case has been selected to evaluate the performances of the method described in the previous section since it includes both liquid phase and ice phase precipitation.

It is observed on figure 22 giving the flight tracks of the two aircraft that we flew almost parallel to the wind most of the time during the straight-line patterns, which is a favourable configuration for the method.

The vertical wind components are shown as arrows on the vertical cross-section of Fig. 32 with the radar reflectivity (contours). The reflectivity field shows the typical feature of stratiform-like precipitation, with a well-defined bright-band at around 1.3 km altitude, indicative of the layer where ice crystals melt. The  $(Vt+w)$  field shows the expected dynamic pattern, with velocities (modulated by the vertical air motion) of around  $-4$  to  $-5$   $\text{ms}^{-1}$  in liquid phase (below the melting layer),  $-1$  to  $+0.2$   $\text{ms}^{-1}$  in ice phase. On the upper-right part of the figure slightly larger negative values are retrieved in the lower part of the ice cloud and smaller negative values in the upper part of the ice cloud. This is likely indicative of either the presence of smaller ice crystals (thus falling at a smaller terminal fall speed) or larger upward air motions in the upper part of the ice cloud. Also, in this part of the cloud  $(Vt+w)$  ranges from  $-0.4$  to  $0.2$   $\text{ms}^{-1}$ . After a careful inspection, it is found that these positive values of  $(Vt+w)$  are correlated with the strongest small-scale reflectivity structures within this part of the cloud (not shown). In these small regions, the upward motions are sufficient to compensate for the sedimentation of precipitation and then lead to an enhancement of ice crystal growth.

In order to separate the liquid and ice phases, we derive an estimate of the  $0^\circ\text{C}$  isotherm altitude using the temperature measurements taken from the two soundings performed when taking off and landing. Another indirect way to estimate the  $0^\circ\text{C}$  isotherm altitude is to look at the height of the radar “bright band” (radar signature of the melting layer) in the vertical cross-sections of radar reflectivity. The  $0^\circ\text{C}$  isotherm is located just above the bright band.

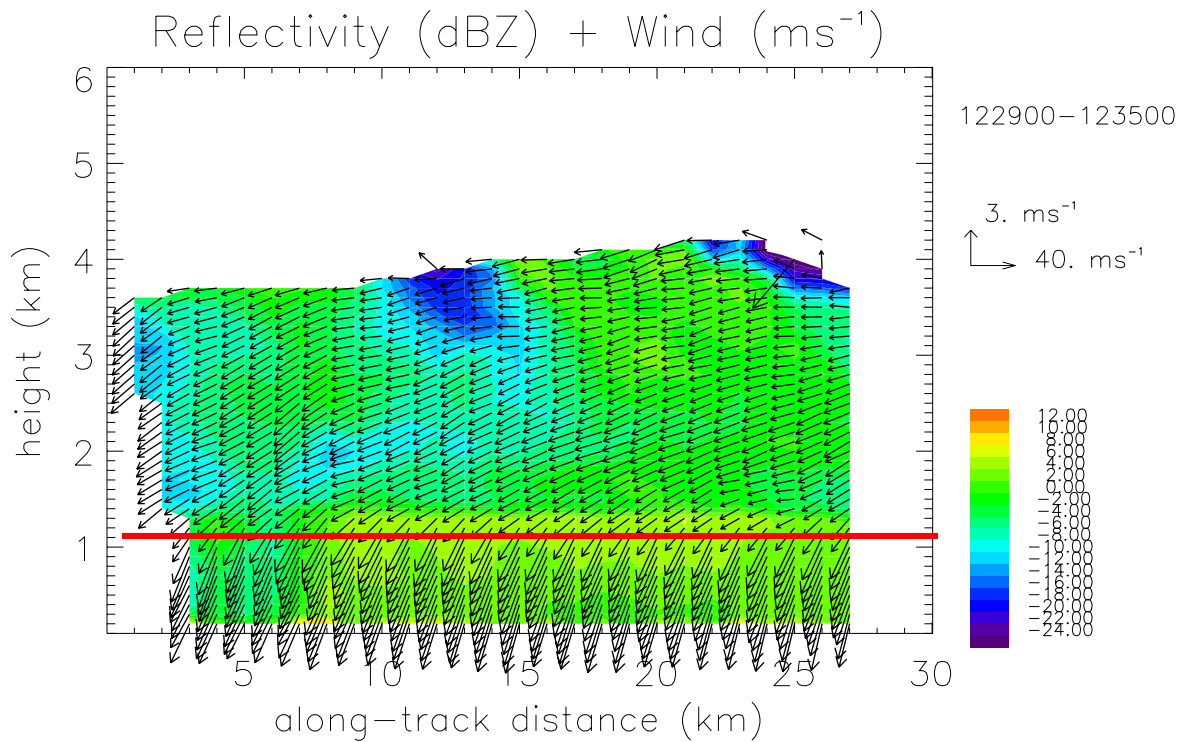
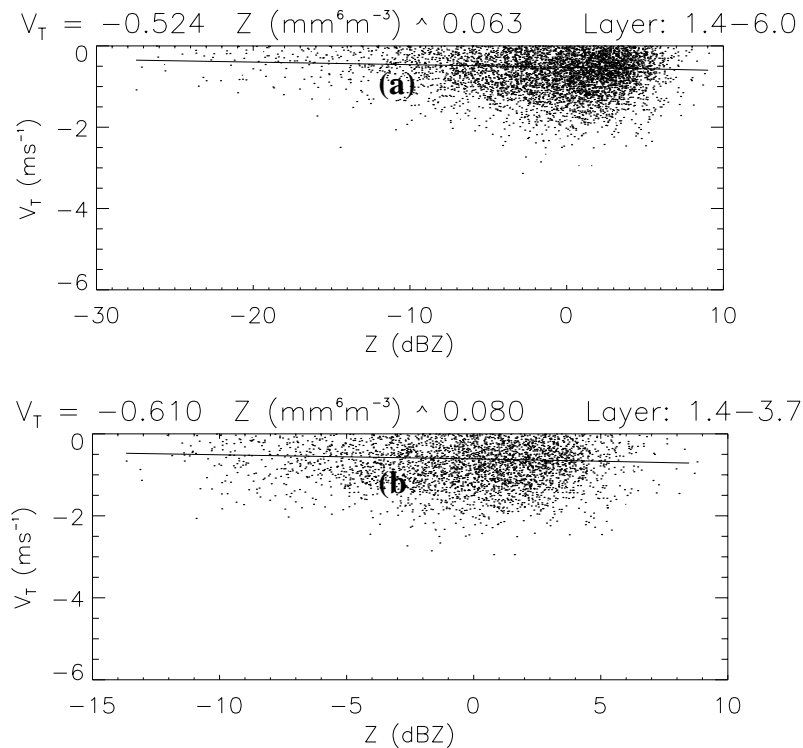
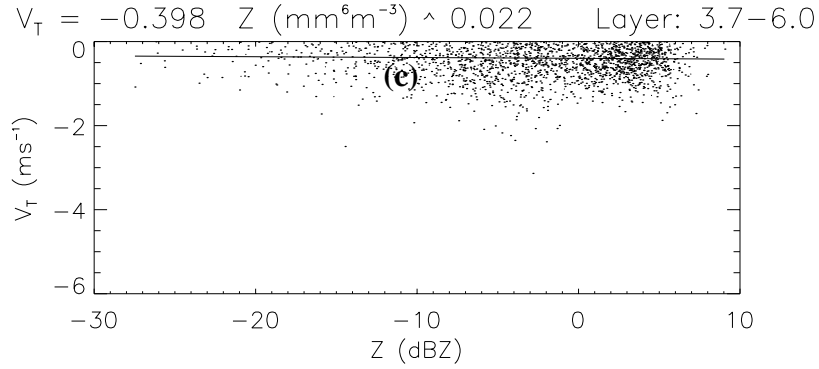


Figure 32 : Vertical cross section of reflectivity (contours) and 2D particle velocity (including fall speed) for the time span 122900-123500 UTC on 13 March 2001. Only one arrow out of three is drawn.

Fig. 33a shows the statistical relationships obtained in ice phase by processing the whole 13 March 2001 flight (from 1215 to 1350 UTC). In order to allow future comparisons with microphysical in situ relationships, a density correction factor  $f(z) = (\rho/\rho_0)^{0.4}$  has been applied to each  $(V_T+w)$  estimate (Foote and Du Toit 1969).





*Fig. 33 :  $V_t$ - $Z$  relationships in ice phase : (a) for the whole ice cloud, (b) for the lower part of the ice cloud (from 1.4 to 3.7 km height), and (c) for the upper part of the ice cloud (from 3.7 to 6 km). Also given are the coefficients of relations ( solid curves) on top of each panel.*

The statistical relationship estimated in ice phase (Fig. 33a) shows that the terminal fall velocity increases with reflectivity, as expected, with a value of  $-0.52 \text{ ms}^{-1}$  for a  $0 \text{ dBZ}$  reflectivity. These values appear reasonable for ice crystal fall speeds. The relatively large scatter around the fitted curve is attributed to the contribution of the vertical air motions for each estimate of the terminal fall velocity.

It must be noted that when processing the whole volume of ice, it is implicitly assumed that there is a single ice particle type, which is probably wrong most of the time. In order to evaluate the degree to which the ice type changes with height within this nimbostratus cloud, we separate in what follows the volume of ice into two sectors : the lower part (from 1.4 to 3.7 km) and the upper part (from 3.7 to 6 km) of the ice cloud. Then, the statistical relationships are computed for each sector. It is obtained that larger (smaller) terminal velocities are found in the lower (upper) part of the ice cloud (Fig. 33b and 33c). This is consistent with the presence of larger (smaller) ice crystals in the lower (upper) part of the cloud, which likely reflects the growth of the ice crystals through aggregation while ice crystals fall, as is generally encountered in the literature (e.g., Marecal et al. 1993). This result indicates that further studies are needed in order to take into account the variability of the statistical relationships with height.

The relationship obtained in liquid phase (not shown) are comparable to the relationships obtained for frontal cyclones by Protat et al. (2002). Nevertheless, the radar reflectivity in rain is not corrected for attenuation yet. Therefore the statistical  $V_t$ - $Z$  relationship in rain may be significantly biased in the present case. Work is under progress to correct the radar attenuation by taking advantage of the two different optical paths travelled by the two radar beams within the same water cloud.

The last step of the retrieval of the dynamic properties consists in subtracting terminal fall velocity (using the radar reflectivity field and the statistical relationships) from the  $(V_t+w)$  field in order to access the 2D wind field. Interesting features are recovered. Maximum upward motions of around  $0.8 \text{ ms}^{-1}$  are retrieved in the area where reflectivities are strongest. In the liquid water part of the cloud, slightly downward motions dominate, with however slight small-scale updrafts in some parts, which is typical of mean vertical wind profiles in stratiform-like precipitation. It must be recalled however that attenuation is not corrected yet in the liquid water layer, which biases the estimate of  $V_t$  (and in turn the estimate of  $w$ ) in the present case.



## 4. General Conclusion

The initial objectives of the campaigns, which were to provide an extended data base, and develop new analysis methods have been met despite some problems with system operation.

Flights have been done involving for the first time airborne radar and lidar observations from the same platform. A reference to these measurements was given by carefully elaborated in situ measurements, involving during the Brest campaign a new sonde (Nevzorov) from GKSS to measure separately total water (ice + liquid) and liquid water contents. Important results have been obtained from a first analysis of the data and comparisons.

The analyses performed on CLARE data have emphasised the capabilities of combined radar and lidar measurements to

- study properties of iced clouds at mid-latitudes over their vertical extent
- retrieve microphysical and dynamical properties in such clouds from combined radar-lidar analysis, as far as water clouds are not altering transmission
- compare with in situ measurements

Measurements are showing limitations to retrieve water cloud properties due to reduced penetration of lidar beam in dense water clouds and limited radar sensitivity to small particles in semi-transparent ones. This last case can however be somewhat considered as an advantage to discriminate super cooled water layers.

Important features such as

- the existence of thin super-cooled water layers embedded in mixed phase clouds (altostratus),
- seeding super-cooled layers
- the evidence of drizzle in most stratocumulus clouds, especially in the convective updrafts

have been observed as expected (or more than expected in the case of super-cooled layers).

Two basic algorithms have been developed and tested. The direct analytic algorithm which relies on the hypothesis that the particle size distribution (PSD) is of gamma type, has been shown to lead to good results, as long as the PSD is monomodal and the multiple scattering in lidar and non-Rayleigh scattering in radar can be corrected. Impact of size distribution needs further analysis, as well as scattering corrections which can be made in an iterative process. Both limitations can be overcome using the statistical algorithm and the normalised PSD, provided adapted power laws can be used. Both algorithms may be further improved and further comparisons need to be performed.

It has been shown that the dynamics of ice particles in the clouds in relation with their size could be further assessed from the combined measurements using direct Doppler information and retrieved microphysics.

Tests have been done for a better presentation of the geometrical model technique to estimate the in-situ reflectivity and check for consistency with radar measurements. This analysis has emphasised the need to use appropriate mass-size models to process 2D in situ probe data.

For the next experiment we would recommend to :

- fly into raindrop layer for a comparison of observation and calculations in the simplest condition (quasi sphere with known density).
- fly FSSP + 2DC + 2DP and Nevzorov again to directly measure the ice water content for validation without any assumption
- cross-check in situ mass derived from size distributions with direct measurements

The microphysics and dynamics of clouds have been investigated using data from the dual-beam cloud radar, and lidar. Further work is to be done to improve these algorithms and analyse further cases in order to investigate the interaction between the microphysics and dynamic processes.

## 5. References

- Bakan, S., J. Schlicht, H.-D. Hollweg, and L. Fiedler (2001): Remote sensing of temperature and atmospheric constituents from surface based FTIR measurements. *Smith, W.L. and Y.M. Timofeyev (Eds.), IRS 2000: Current Problems in Atmospheric Radiation*. A. Deepak Publ., Hampton, Va., USA, **147**, 1125-1128
- Brown P. R. A. and P. Francis, 1995 : Improved measurements of the ice water content in cirrus using a total-water probe, *J. Atmos. Ocean Tech.*, **12**, 410-414.
- Dreyer, M. and S. Bakan (2001): Ground-based remote sensing of cloud properties from multi-spectral FTIR measurements. *Smith, W.L. and Y.M. Timofeyev (Eds.), IRS 2000: Current Problems in Atmospheric Radiation*. A. Deepak Publ., Hampton, Va., USA, **147**, 989-992
- Fiedler, L. and S. Bakan (2001): Measurements of sea surface reflectivity in the IR window region. *Smith, W.L. and Y.M. Timofeyev (Eds.), IRS 2000: Current Problems in Atmospheric Radiation*. A. Deepak Publ., Hampton, Va., USA, **147**, 1015-1017
- Foote, G. B., and P. S. Du Toit, 1969: Terminal velocity of raindrops aloft. *J. Appl. Meteor.*, **8**, 249-253.
- Fox and A. J. Illingworth, 1997 : The potential of a spaceborne cloud radar for the detection of stratocumulus clouds, *J. Appl. Meteor.*, 485-491.
- Francis, P. N., P. Hignett, and A. Macke, 1998: The retrieval of cirrus cloud properties from aircraft multi-spectral reflectance measurements during EUCREX'93, *Q. J. R. Meteorol. Soc.*, **124**, pp. 1273-1291.
- Hitschfeld, W. and J. Bordan, 1954: Errors inherent in the radar measurement of rainfall at attenuating wavelengths. *J. Meteor.*, **11**, 58-67.
- Heymsfield A. J. and J. Iaquinta, 2000 : cirrus crystal terminal velocities, *J. Atmos. Sci.*, **57**, 916-938.
- Intrieri J., G. L. Stephens, W. L. Eberhard, and T. Uttal, 1993 : « A method for determining cirrus cloud particles size using lidar and radar backscatter technique » *J. Appl. Meteor.*, 1074-1082.
- Kendall, M.G. (1980): *Multivariate analysis*. (2nd ed.), Griffin, London.
- Klett J.D., 1981, Stable Analytical Inversion Solution for Processing Lidar Returns, **20**, 2, 211-220.
- Khvorostyanov V. I. and J. A. Curry, 2002 : Terminal velocity of droplets and crystals : Power laws with continuous parameters, *J. Atmos. Sci.*, **59**, 1872-1884.
- Liao and K. Sassen, 1994 : Investigation of relationships between Ka band radar reflectivity and ice and liquid water content, *Atmos. Res.*, **26**, 213-228.

- Lee, W.-C., P. Dodge, F. D. Marks, and P. H. Hildebrand, 1994: Mapping of airborne Doppler radar data. *J. Atmos. Oceanic Technol.*, **11**, 572–578.
- Liu C.-L. and A. J. Illingworth, 2000 : Toward accurate retrievals of ice water content from radar measurements of clouds, *J. Appl. Meteor.*, 39, 7, 1130-1146.
- Locatelli J. D. and P. Hobbs, 1974 : Fall speeds and masses of solid precipitation particles, *J. Geophys. Res.*, 79, 15, 2185-2206.
- Marécal, V., D. Hauser, and F. Roux, 1993: The NCFR observed on 12-13 January 1988 during the MFD/FRONTS87 Experiment. Part II: Microphysics. *J. Atmos. Sci.*, **50**, 975-998.
- Matrosov S., T. Uttal, J. B. Snider and R. A. Kropfli, 1992 : Estimation of ice cloud parameters from ground-based infrared radiometer and radar measurements, *J. Geophys. Res.*, 97, 11 567-11 574.
- Matrosov S., A. J. Heymsfield, R. A. Kropfli, B. E. Martner, F. Reinking, J. B. Snider, P. Piironen, and E. W. Eloranta, 1998 : Comparisons of ice cloud parameters obtained by combined remote sensor retrievals and direct methods, *J. Atmos. Ocean Technol.*, 15, 184-196.
- Matrosov S. Y. and A. J. Heymsfield, 2000 : Use of Doppler radar to access ice cloud particle fall velocity-size relations for remote sensing and climate studies, *J. Geophys. Res.*, 105, 22 427-22 436.
- Morrison, D.F. (1990): *Multivariate statistical methods*. (3rd ed.), McGraw Hill, N.Y., USA
- Platt C. M. R., D. M. Winker, M. A. Vauhahn, and S. D. Miller, 1999 : Backscatter-to-extinction ratios in the top layer of tropical mesoscale convective systems and in isolated cirrus from LITE observations, *J. Appl. Meteor.*, 38, 1330-1345.
- Platt C. M. R., S. A. Young, R. T. Austin, G. R. Patterson, D. L. Mitchell and S. D. Miller, 2002 : LIRAD observations of tropical cirrus clouds in MCTEX. Part I: optical properties and detection of small particles in cold cirrus, 59, 22, 3145-3162.
- Protat, A., Y. Lemaître, and D. Bouniol, 2002 : Terminal fall velocity and the FASTEX cyclones, Submitted to the *Quart. J. Roy. Meteor. Soc.*.
- Protat, A., Y. Lemaître, D. Bouniol, and R. A. Black, 2000: Microphysical observations during FASTEX from airborne doppler radar and in-situ measurements. *Phys. Chem. Earth (B)*, **25**, 1097-1102.
- Protat, A., Y. Lemaître, and G. Scialom, 1997: Retrieval of kinematic fields using a single-beam airborne Doppler radar performing circular trajectories. *JAOT*, **14**, 769-791.
- Pruppacher H. R. and J. D. Klett, 1997 : Microphysics of clouds and precipitations, Kluwer, 997 pp.

- Ricchiazzi, P., S. Yang, C. Gautier, and D. Sowle (1998): SBDART: A Research and Teaching Software Tool for Plane-Parallel Radiative Transfer in the Earth's Atmosphere. *Bull. Amer. Meteor. Soc.*, **79**, 2101-2114.
- Rogers R. R. and M. K. Yau, 1996 : A short course in cloud physics, Butterworth and Heinemann, 290 pp.
- Sassen K., 1987 : Ice cloud content from radar reflectivity, *J. Climate Appl. Meteor.*, 29, 153-163.
- Sassen K. and L. Liao, 1996 : Estimation of cloud water content by W-band radar, *J. Appl. Meteor.*, 35, 932-938.
- Schneider T. L. and G. L. Stephens, 1995 : Theoretical aspects of modelling backscattering by cirrus ice particles at millimeter wavelength, *J. Atmos. Sci.*, 52, 4367-4385.
- Stamnes, K., S.-C. Tsay, W. Wiscombe, and K. Jayaweera (1988): Numerical stable algorithm for discrete-ordinate-method radiative transfer in multiple scattering and emitting layer media. *Appl. Opt.*, **27**, 2502-2509.
- Testud, J., S. Oury, R. A. Black, P. Amayenc, X-K Dou, 2001: The Concept of “Normalized” Distribution to Describe Raindrop Spectra: A Tool for Cloud Physics and Cloud Remote Sensing. *J. Appl. Meteor.*, **40** (6), 1118–1140.
- Testud J., E. Le Bouar, E. Obligis, and M. Ali Mehenni, 2000: The rain profiling algorithm applied to polarimetric weather radar, *J. Atmos. Oceanic Technol.* **17**, No 3, 332-356.
- Tinel C., J. Testud, A. Guyot and K. Caillaud, 2000: Cloud parameter retrieval from combined remote sensing observations, *Phys. Chem. Earth (B)*, No 10-12, 1063-1067.
- Tinel C. and C. Duroure, 29 Janv 2002, Toulouse, Atelier Experimentation et Instrumentation de L'INSUE
- Tinel, C., J. Testud, A. Protat, and J. Pelon, 2002: Combined radar and lidar observations for the retrieval of radiative and microphysical properties in ice clouds. Preprints, 11<sup>th</sup> Conference on Cloud Physics, AMS, Ogden, UT, USA, 3-7 June 2002.
- Tinel C., 2002 : Restitution des propriétés microphysiques et radiatives des nuages froids et mixtes à partir des données du système RALI (Radar-Lidar), thèse de l'Université Pierre et Marie Curie, 220pp.
- Ulbrich, C. W., 1983: Natural variations in the analytical form of the drop size distribution. *J. Clim. Appl. Meteor.*, **22**, 1764-1775.
- Virolainen Ya.A., H. Grassl, S. Bakan, H.-D. Hollweg, A.V. Polyacov, and Y.M. Timofeyev (2002a): Ground-based thermal Fourier-spectrometer remote-sensing experiment. *Submitted to Izvestiya, Atmospheric and Oceanic Physics*.
- Virolainen Ya.A. and S. Bakan (2002b): Ozone determination in different atmospheric layers using OASIS ground-based emission measurements. *In preparation*.

Wang Z. and K. Sassen, 2002 : Cirrus cloud Microphysical property retrieval using lidar and radar measurements. Part I : Algorithm description and comparison with in situ data, J. Appl. Meteor., 41, 218-229.

## ANNEX A INSTRUMENT CHARACTERISTICS

### Ground-based Instruments (Phase 1)

Ground-based systems have taken an active part to the first campaign held in Brest. No ground-based measurement was made in the second phase, as this phase was focused on a much broader area.

They have allowed to collect a complete data set obtained from ground-based lidar and radar to describe cloud properties and survey of dynamics into the cloud, in favourable meteorological situations. They are

- The Cloud Doppler radar MIRACLE operating at  $\lambda = 3.2 \text{ mm} - 94.9 \text{ GHz}$ - (GKSS)
- The Vaïssala ceilometer operating at 905 nm (KNMI)
- The backscattering lidar SLIM operating at  $\lambda = 532 \text{ nm}$  (IPSL)
- Radiometry from KNMI (including a camera for a whole sky survey)
- The Fourier Transform spectrometer OASIS (MPI)



*Figure A1 : Implementation of the ground-based instruments in Brest airport area. The shelter for the meetings is seen in the front with the CT75 ceilometer on its left and the GKSS radar behind. The OASIS FTS is located behind the mobile lidar van on the right of the shelter.*

#### **Ground-based Radar MIRACLE (GKSS)**

Manufacturer: CPI

Wavelength: 3.2 mm (94.92 GHz)

Peak Power (EIA) : 1.7 kW

Pulse repetition frequency : 50Hz-80 kHz

Duty cycle : 1.2 %

Antenna diameter: 120 cm, 2 channels (two-polarisations transmit/or receive), Doppler processing

Observation angle: elevation: 0 to + 90 deg (manual adjustment)

Measurement range: 0-15 km

Range resolution : 15-300 m  
Implementation : transportable shelter

**Ground-based backscatter lidar SLIM (IPSL/SA)**

Manufacturer: IPSL  
Wavelength: 532 nanometer (Nd-Yag laser)  
Energy : 20 mJ @10Hz  
Receiver type: 30 cm diameter telescope, 2 channels (cross-polarisations) Photomultiplier tubes, responsivity at 532 nm: 65 A/W  
Observation angle: zenith  
Measurement range: 0-30 km  
Range resolution: 15 m  
Integration time: 10 s  
Interface: PC  
Implementation : van

**CT75K ceilometer (KNMI)**

Receiver type: Silicon Avalanche Photodiode, responsivity at 905nm: 65 A/W  
Manufacturer: Vaisala  
Wavelength: 905 nanometer (InGaAs laser diode) +/- 5 nm at 25 °C  
Observation angle: elevation: 0 to +90 deg is possible  
Measurement range: 0 to 75000 ft (0-22.5 km)  
Range resolution: 100 ft (30 m)  
Integration time: 30 s  
Interface: PC  
Dimensions: 1.210 m x 0.765 m x 0.510 m  
Weight: 83 kg

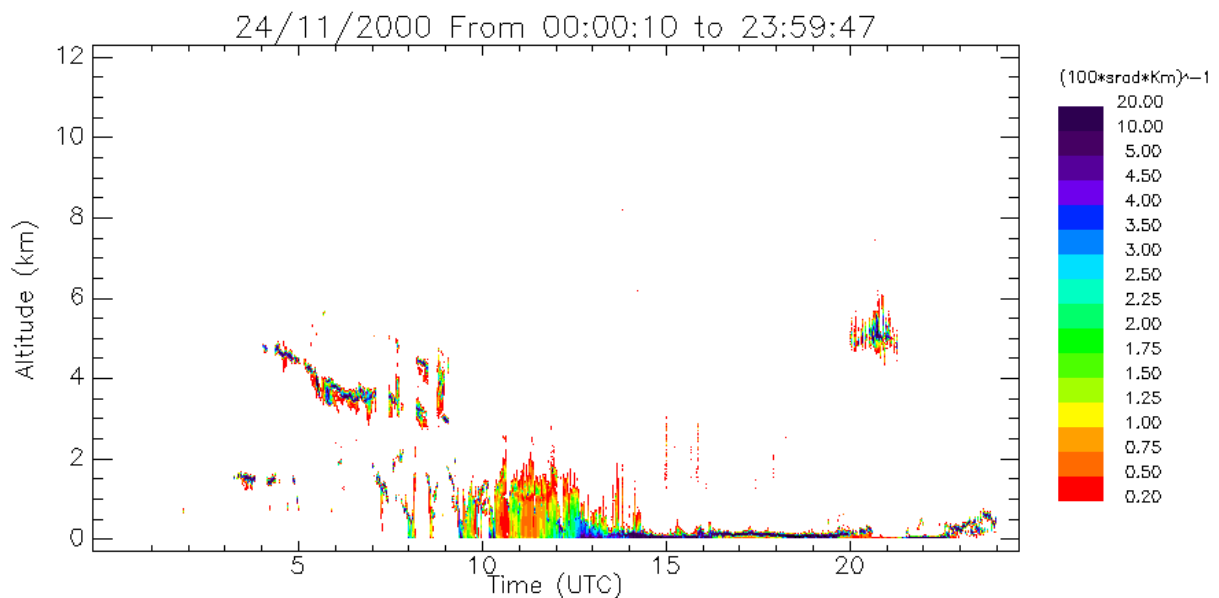


Figure A2 : Backscattering coefficient measured on November 24, 2000 in Brest with the KNMI CT 75K. Clear air is observed between 10 UTC and 20 UTC.

### **Heimann IR radiometer (KNMI)**

Receiver type: IR radiation pyrometer, lens system K6

Manufacturer: Heimann Optoelectronics

Spectral response: 9.6 to 11.5 micrometer

Observation angle: 0-90 deg

Opening angle: 50 mrad

Temperature range: -50 to + 50 °C

Integration time: 1 s

Temperature resolution: 0.5 °C

Interface: RS 232

Dimensions: 161 x 52 x 52

Weight: 0.45 kg

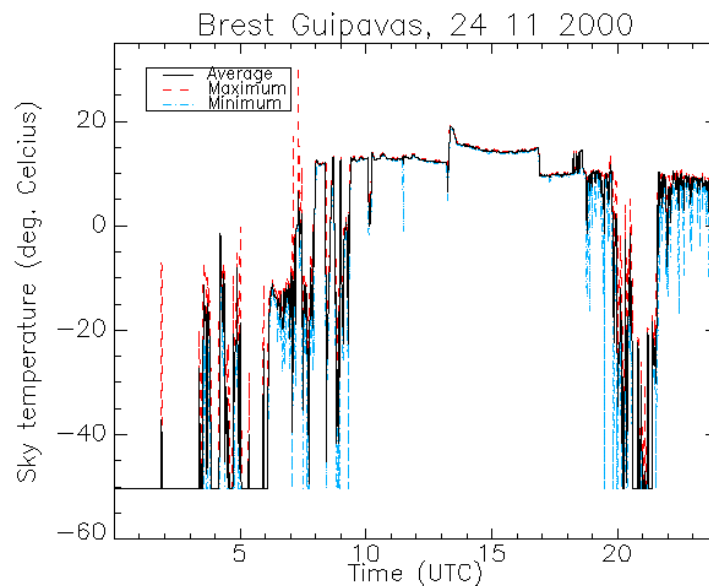


*Figure A3 : Brightness temperature measured on November 24, 2000 in Brest with the KNMI IR radiometer. Higher brightness temperatures correspond to clear air areas observed by the CT75K*

### **Time-lapse Cloud Video camera (KNMI)**

Camera: Panasonic colour video camera, type WV-CL700. Lens:

WV-LA2.8, FOV 107 ° H, 88 ° V

Recorder: Panasonic S-VHS time-lapse recorder, type NVFS-88EG.

Recording speed: 4 frames/second.

### **The Fourier transform spectrometer vis-near IR FTIR OASIS (0.7-15 µm) (MPI)**

The measuring system OASIS (Ocean-Atmosphere Sensing Interferometer System) covers both, the thermal (TIR) and the near infrared spectral range (NIR) between 600 and 12000  $\text{cm}^{-1}$  with a maximum spectral resolution of 1  $\text{cm}^{-1}$ . The system is based on a BOMEM MR154 FTIR Interferometer. Its spectral resolution allows to utilise the downwelling radiation in sufficiently transparent micro-windows of the spectral ranges of thermal emission ( $< 3000 \text{ cm}^{-1}$ ) and of near infrared solar scattering ( $> 2400 \text{ cm}^{-1}$ ) for the derivation of cloud properties, as their combination contains more information than either of the spectral ranges alone.

The data for this study were collected during two weeks of the campaign CLARE2000 at Brest, France. The data set consists of more than 7600 single spectra of zenith measurements with a spectral resolution of  $1 \text{ cm}^{-1}$  and a temporal resolution of 4 seconds. To avoid serious damage of the input mirror of the system, measurements could only be performed under non-raining conditions, which leads to some larger time gaps in the data set.

In order to eliminate the influence of the atmospheric gases as far as possible, as a first step the continuous spectra are reduced to a set of 45 micro-window channels. EOF analysis of the micro-window signal is used to determine both, the spectral regions with significant information and the characteristic spectral signature of different cloud types, as well. A classification of the spectra related to observed cloud types has been approached by means of cluster analysis. The cloud microphysical properties are to be retrieved by iterative calculations with radiative transfer models.

In order to cover both, the thermal and the near infrared spectrum, it is fitted with two detector units, which are scanned sequentially. That leads to a time gap of two seconds between the two spectral ranges. Due to the spatial resolution of the instrument, this is not a problem observing clouds with view to the zenith. For continuous calibration, the system is equipped with two blackbody units of high emissivity for the thermal and an integrating sphere for the near infrared spectral region. The calibration of the reference sources is traceable to national standards. Both, the calibration and the measurement at arbitrary positions are performed automatically. The major technical data are summarized in Table A1.

|                     |  |
|---------------------|--|
| FTIR Interferometer | BOMEM MR154  |
| Detector Type       | MCT (TIR)<br>InSb (NIR)                                  |
| Spectral Range      | $600 - 12000 \text{ cm}^{-1}$<br>$0.83 - 16 \mu\text{m}$ |
| Spectral Resolution | $1 - 128 \text{ cm}^{-1}$                                |
| Temporal Resolution | $4 - 1/32 \text{ s}$<br>(2 scans per detector)           |
| Spatial Resolution  | $2.5^\circ$ IFOV   |
| Black Body Unit     | $< 0.05 \text{ K}$                                       |
| Temperature Error   |  |
| BBU Emissivity      | $> 0.999$  |

Table A1: *OASIS Technical Data.*

Figure A4 gives an overview of the system topology.

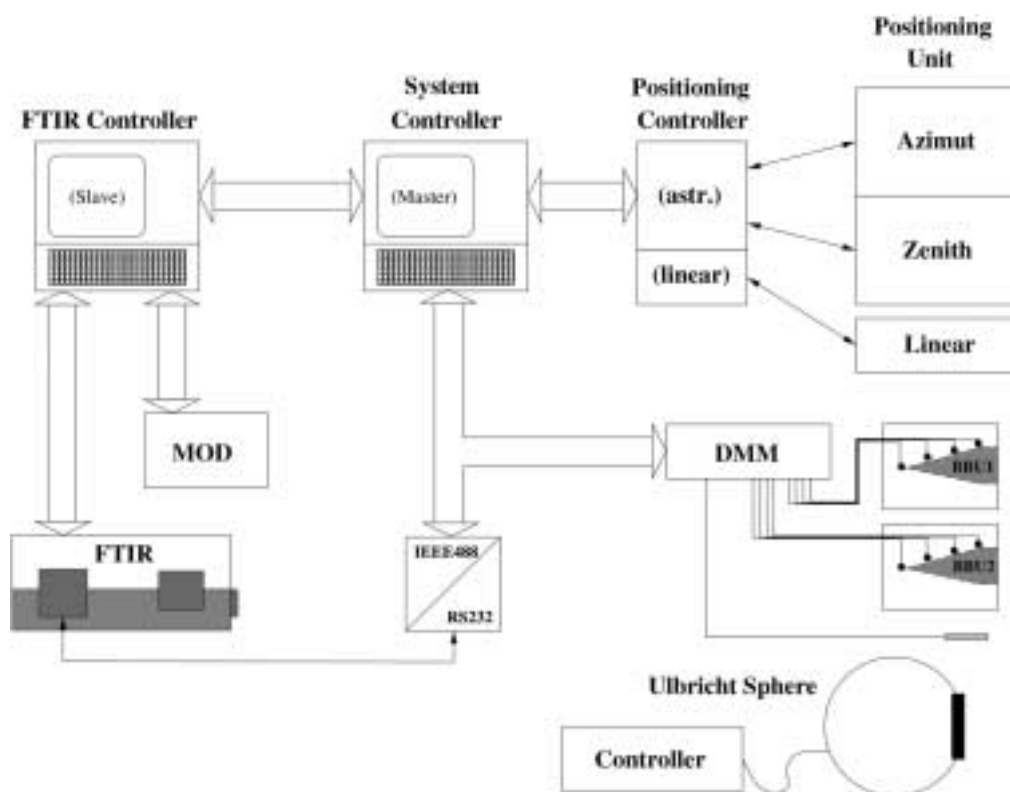


Figure A4: OASIS System Map.

The system has been successfully applied in various studies. In clear sky situations, the derivation of boundary layer temperature and water vapour profile becomes possible with satisfactory accuracy and an unprecedented time resolution (Bakan et al., 2001). In addition, it was shown in Virolainen et al. (2002a) that also the column content of Methane and N<sub>2</sub>O may be derived. Recently, the derivation of ozone profile information could be shown (Virolainen and Bakan, 2002b). OASIS has also been used from an ocean pier and from ship board to estimate sea surface emissivity and its influence on the determination of sea surface temperatures from downward looking radiometer measurements (Fiedler and Bakan, 2001).

### Channel Selection

Investigations of cloud properties are only possible in spectral regions with small absorption by atmospheric gases (Figure A5).

The red line shows a MODTRAN calculation of the atmospheric transmissivity for a typical midlatitude summer atmosphere, which represents the worst case for midlatitude measurement conditions because of the large content of water vapour. Especially, this is a problem in the spectral region between 800 and 1200 cm<sup>-1</sup> due to a large amount of absorption lines in combination with the H<sub>2</sub>O continuum absorption, which reduces the transmissivity to values below about 70 %.

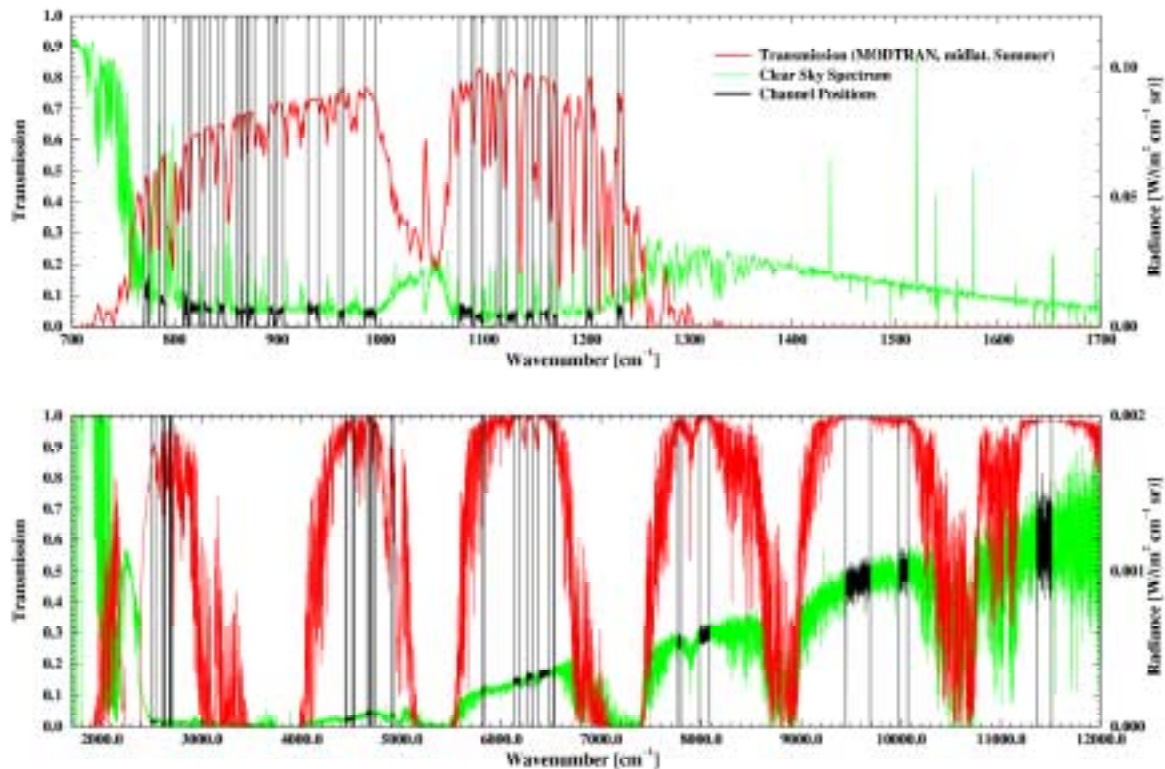


*Figure A 5: Selected spectral channels (delimited by the vertical lines) in the transmission windows as obtained from MODTRAN calculations (red curve and left ordinate). Green curve is giving measured radiance values in clear air (right ordinate, a scaling factor of 60 has been applied to the lower figure).*

Considering calculated and measured spectra, a sample of 45 spectral micro-window channels with satisfactory transmissivity are defined, of which 23 are located in the thermal and 22 in the near infrared region. The green line in Figure A5 shows an exemplary clear sky spectrum. The observation channels are highlighted in black colour, and the channel boundaries are depicted with black bars. The appropriate choice of spectral channels does not only reduce the disturbance of the atmosphere on the cloud observations. It also reduces both, the noise level by averaging over several spectral values and the amount of data. This is an advantage for operational data processing.

## ANNEX B INSTRUMENT CHARACTERISTICS

### Airborne Instruments (Phases 1 & 2)

#### Merlin Aircraft (Meteo-France)/In situ sondes

Basic measurements (Météo-France)

- Temperature
- Humidity
- Wind
- Liquid water (bulk water) Geiger probe
- Radiometry (Eppley pyranometers and pyrgeometers)

*Specific measurements (GKSS –phase 1-, LAMP-phase 2-)*

For the determination of the microphysical properties, the MERLIN IV of Météo-France has been equipped with in situ sondes. In phase 1, the GKSS cloud particle measuring system consisting of several sizing probes and one probe to estimate the Liquid Water Content (LWC) and the Total Water Content (TWC). The instrumentation is described among other things in more detail at the GKSS microphysics group's home page (<http://w3.gkss.de/Pms/microphy.htm>). The MERLIN was equipped simultaneously with 4 particle sizing probes and one Nevzorov probe.

The probes have been carefully calibrated before and during the campaign by the laboratories responsible of the measurements. The main characteristics of the probes are given in Table A1.

| Instrument             | Purpose                           | size range / $\mu\text{m}$ |
|------------------------|-----------------------------------|----------------------------|
| PMS FSSP-100           | cloud particle properties         | 2.0 – 49.0                 |
| PMS OAP-2D2-C          | cloud / drizzle particles         | 25.0 – 800.0               |
| PMS OAP-2D2-P          | precipitation particles           | 200.0 – 6400.0             |
| Nevzorov LWC/TWC probe | LWC/IWC measurements              | -                          |
| SEA M200               | data acquisition system<br>(GKSS) | -                          |

*Table B1: Microphysical Instruments installed onboard the Merlin IV of Meteo-France for the Clare2000 campaign*

During all the 2001 flights in phase 2, the MERLIN aircraft was equipped with its standard dynamical and thermodynamics set of probes (Meteo-France) including INS and GPS positioning as from phase 1. The Merlin was equipped with the same type of sondes for small and medium size particles :

- The standard FSSP100 probe
- The Cloud Dimensional Probe (Knollenberg) sizes the particles from 20 to 600 micrometers ( 20 micrometers bin size) using the maximal dimension of the shadow of the particle perpendicularly to the flight direction whatever the particle shape.

- The 2DC imaging probe which allows different estimations of the characteristic size of the crystal. In the presented results we are used the maximal dimension perpendicular and parallel to the flight direction, the squared surface of the crystal image to estimate different characteristic size. The pixel size of the hydrometeor image is 25 micrometers.

These probes use the forward scattering intensity to estimate a size spectrum of the small hydrometeors (for the FSSP100 the spectrum is estimated between 3 to 47 micrometers diameters with a 3 micrometers bin size). Their principle of measurement is designed for spherical particles. The PMS OAP-2D2-P and Nevzorov were not used. A Fast FSSP probe was used to improve counting performance for small particles.

The liquid water content of water droplets (diameter smaller than 50 micrometers) are estimated using :

- The King probe based on the cooling effect of small hydrometeor impingements on a hot wire detects mainly the super-cooled droplets.
- The Gerber probe use forward scattering diffusion and detect (like the FSSP probe) all the hydrometeors.

These two probes are sampled with 200 Hz time (or 50 centimetres space ) resolution. The LWC data (averaged at 1 Hz) have been compared with the size integrated FSSP estimation data during the 12/03/01 case. Good linearity and quantitative agreement better than 10% are obtained for all the probes in super-cooled regions. In small crystals regions, large scatter occurs between the King probe and the other ones.



*Figure B1 : GKSS In situ probes equipping the Merlin IV in Brest*

**ARAT (CNRS/CNES/Météo-France/IGN) (<http://www.dt.insu.cnrs.fr>) (phases 1 & 2)**

Basic measurements (INSU/DT), temperature, humidity, wind, radiometry (Eppley pyranometers and pyrgeometers) were complemented by remote sensing instruments from IPSL : the backscatter lidar LEANDRE 1 (IPSL/SA) operating at 532/1064 nm, dual polarisation and the cloud radar RASTA (IPSL/CETP) operating at 94.92 GHz, dual beam antenna.

### **RASTA Cloud Radar (CETP)**

During the CLARE 2000 campaign, the airborne version of RASTA developed at CETP has been operated. It is composed of the 95 GHz pulsed radar, emitting a 1.8 kW peak power, with a range resolution of 60 m (tunable), and a PRF of 25 kHz. It includes a dual-beam emission (antennas are 30.5 cm horn lens, 0.7° beamwidth, with a 47 dB gain), with a nadir-pointing beam, and a beam pointing 40° fore in the direction of the aircraft heading. It has been first installed on the CNRS/Meteo-France/CNES research aircraft (ARAT) in October 2000. After some modifications of the emitter to solve operating problems observed during the first phase, it has been re-installed in March 2001. The airborne version has been validated during the first phase of the CLARE campaign, which was held in November 2000 in Brest, France. Its sensitivity was found to be -23 dBZ at a 1 km range.

### **LEANDRE backscatter lidar (SA/LMD)**

LEANDRE 1 is a backscatter lidar based on the use of a Nd-Yag laser source operating in the visible (532 nm) and near infrared (1064 nm) at a 12 Hz pulse repetition rate. The signal emitted at 532 nm is linearly polarized and the backscattered signal is analysed at both vertical and horizontal polarisations. Lidar signal is due to scattering by atmospheric molecules and particles. Scattering by molecules and droplets (or crystals) correspond to different regimes.

Rayleigh scattering by molecules can be used as a reference in the visible as the corresponding signal can be easily measured.

In the 532 nm parallel polarization channel (polarization identical as the emitted one) and 1064 nm channel, the lidar signal is normalized to atmospheric scattering at an altitude close to the aircraft, or further down where a clear air layer can be found. In the case such an area cannot be found an average normalisation coefficient is used.

The cloud radar RASTA and the backscatter lidar LEANDRE are independent systems. Further developments are currently performed to combine RASTA and LEANDRE measurements in a more integrated way. This will allow an easier deployment on several aircraft for future campaigns.

## ANNEX C

### RETRIEVAL OF PARTICLE SIZE AND WATER CONTENT FROM RADAR – LIDAR ANALYSIS

In cold clouds, particles are no longer pure droplets but are a mixture of liquid water droplets and ice crystals, possibly aggregating, freezing with different shapes as a function of thermodynamics in the cloud (Pruppacher and Klett, 1997). In clouds at temperature colder than 233 K, only ice crystals are observed. Such crystals are non-spherical and the particle size distribution is usually given in terms of the maximum dimension of the crystal.

Two algorithms have been developed to allow the retrieval of the particle properties from radar and lidar which are described hereafter.

#### A. A statistical algorithm for numerical radar/lidar data inversion (CETP)

Starting from power law relationships between radar reflectivity, lidar backscattering, ice water) liquid content and effective diameter, similar to the ones discussed before, a specific algorithm has been developed at CETP to invert radar and lidar signals (Tinel et al., 2000).

Moments of the particle size distribution are linked to the signal measured by radar (6<sup>th</sup> order moment) or lidar (2<sup>nd</sup> order moment). Assuming a normalised size distribution  $N^*(D)$  defined as

$$N(D) = N_0 * N(D / D_m) \quad (C1)$$

the general expression of the  $i^{\text{th}}$  order moment of the PSD is:

$$M_i^* = M_i / N_0^* = \int N^*(D / D_m) D^i dD = D_m^{i+1} \xi_i \quad (C2)$$

where  $\xi_i$  is the  $i^{\text{th}}$  order moment of the normalized distribution  $N^*(D)$ . So that relationships between two moments of order  $i$  and  $j$  can be established as

$$M_i^* = \left[ \xi_i \xi_j M_j^* \right]_{j+1}^{i+1} \quad (C3)$$

Eq. (C3) shows that the relationship between two normalised moments of orders  $i$  and  $j$  of the PSD is a power law whose exponent is  $(i+1)/(j+1)$ . This relationship only depends on the moments of the normalized PSD. Indeed such a dependence is expected to be weak (as far as gamma distributions are considered), since by definition  $\xi_3 = \xi_4 = \Gamma(4)/4^4$ , which strongly constrains the other moments.

The equivalent radar reflectivity  $Z_e$ , the specific radar attenuation  $K$ , the backscattering coefficient for lidar  $\beta$ , the lidar extinction coefficient  $\alpha$ , can be defined to be proportional to moments of the PSD.

To avoid the use of scattering calculations needed in the analytical approach to derive the extinction coefficient, an inverse model has been developed relying upon a set of power laws relationships relating the radar parameters (reflectivity  $Z$ , attenuation  $K$ ), the lidar parameters (backscattering coefficient  $\beta$  and extinction coefficient  $\alpha$ , and their ratio  $k$ , defined as the phase function at a scattering angle of 180°) and the normalized distribution parameter  $N_0^*$ .

The power laws are defined as

$$\alpha = C_a [N_0^*]^{-d} K^d \quad (C4)$$

for attenuating clouds and

$$\alpha = C_z [N_0^*]^{-b} Z^b \quad (C5)$$

for others, along with

$$IWC = C_i [N_0^*]^{-m} K^m \quad (C6)$$

or

$$IWC = C_j [N_0^*]^{-q} Z^q \quad (C7)$$

Extinction and scattering coefficients for lidar are linked by the linear relationship

$$\beta = f\alpha \quad (C8)$$

where  $f$  is defined by the ratio of the phase function  $P(180)$  at a scattering angle of  $180^\circ$  and the multiple scattering factor  $\eta$  related to lidar detection geometry (Platt, 1973).

Relationships between these parameters are almost impossible to establish directly due to dispersion. Once normalized by  $N_0^*$  as in Tinel et al (2000), the dispersion is minimized, and power law relationships can easily be defined as a function of temperature as shown in Figure C1. It is seen on the Figure that two slopes can be adjusted (a threshold value  $\log(Z/N_0^*) = -8$  defining the limit between both domains) as a function of normalised reflectivity, due to the change in scattering regime corresponding to the increase in size at large  $Z$ .

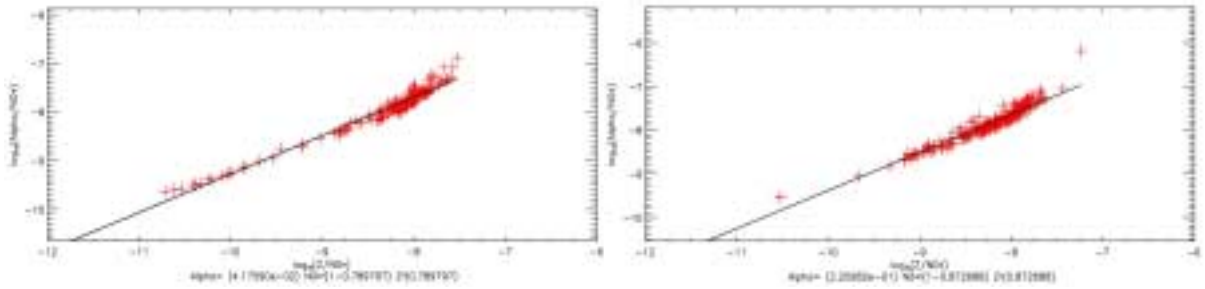


Fig C1. : Examples of the  $\alpha/N_0^*$  versus  $Z/N_0^*$  relationship obtained from the CLARE98 in situ microphysical data set at two temperatures ( $-10^\circ\text{C}$  left figure and  $-14^\circ\text{C}$  right figure).

In the algorithm, the inversion of the measurements was done in parallel for lidar and radar, using relationships (C4) to (C8) as defined from Mie calculations for water clouds and from microphysical data sets gathered from previous campaigns for ice. The ice water content, the radar reflectivity and attenuation and the optical extinction were calculated from in situ measurements made during CLARE'98, CARL'99, CARL-CLARE'2000. CLARE'98 data were analysed assuming a power law for the mass-size relationship (Brown and Francis, 1995), whereas mass was directly obtained from measurements during Carl campaigns. A

global analysis independent of the temperature was performed for ice clouds. (Tinel et al., 2002).

It is difficult to define error bars in the case of this algorithm, as biases may propagate. Simulations have been done to define confidence intervals (Tinel, 2002b), and errors on the retrieved microphysical parameters are of the order of 20% for a SNR of 10 in both radar and lidar measurements assuming no other error source.

Thanks to the similarity between reflectivity and backscattering coefficient exact expressions (written respectively by Hitschfeld and Bordan, 1954 and Klett, 1981), it is possible to write the exact expressions of the radar attenuation and lidar extinction as written by (Testud et al, 2000) :

$$K(r) = \frac{K(r_0)Z_a^b(r)}{Z_a^b(r_0) + 0.46bK(r_0)\int_r^{r_0} Z_a^b(s)ds} \quad (C9)$$

$$\alpha(r) = \frac{\alpha(r_0)\beta_a(r)}{\beta_a(r_0) + 2\alpha(r_0)\int_r^{r_0} \beta_a(s)ds} \quad (C10)$$

where  $r$  is the distance from the radar and  $r_0$  and  $r_1$  the extreme boundaries of the integration length.

To retrieve those two last profiles, the values of  $K$  and  $\alpha$  at  $r_0$  are set from the following constraint:

$$\int_{r_1}^{r_0} \alpha(s)ds = c[N_0^*(r)]^{1-d} \int_{r_1}^{r_0} K^d(s)ds \quad (C11)$$

Combining all equations, it is possible to retrieve the initial condition  $\alpha(r_0)$  through an iterative process initiated with a first guess of  $N_0^*$ . We assume in this calculation that  $N_0^*$  is constant between  $r_0$  and  $r_1$ .  $[r_0, r_1]$  is the integration length corresponding to a distance equal to 5 instrumental gates. The iteration process converges toward a value of  $\alpha(r_0)$ . We also assume that the reflectivity attenuation is negligible in ice clouds. The knowledge of  $\alpha(r_0)$  and  $Z(r_0)$  allows to calculate the value of  $N_0^*(r_0)$  (from the power law relationships), which is equal to the value of  $N_0^*[r_0, r_1]$ .

Once we obtain the  $\alpha$  profile, and an IWC profile, (from  $Z$  and  $N_0^*$ ), it is possible to retrieve an effective radius ( $r_e$ ) profile.

In the data analysed here, we have used the  $Z$ - $\alpha$  version of the algorithm, with a value of  $N_0^*$  segmented along the retrieved profile to account for the variation of temperature with altitude and particles aggregation (Tinel, 2002).

## B. Analytical algorithm (SA/LMD)

In this algorithm, a explicit physical approach based on the use of the lidar extinction and radar reflectivity is presented. Analytical expressions are used which take into account physical relationships between measured quantities and microphysical cloud parameters.

Hexagonal crystals are usually considered as a standard model to calculate radiative properties of ice clouds (Takano and Liu, 1989; Fu, 1996). In a recent paper (Mc Farquhar et

al., 2002), a slightly different formulation for extinction has been proposed to better fit the spectral dependence of the radiance scattered by crystals. As it is equivalent to first order, we will write the extinction cross-section  $\sigma$  for hexagonal crystals in the approximation of geometric optics as a function of the two size parameters of the crystal as (Takano and Liou, 1989)

$$\alpha = IWC \left( A + \frac{B}{D_{ge}} \right) \quad (C12)$$

where A and B are empirical constants ( $A = -6.66 \cdot 10^{-3}$  and  $B = 3.686$ ) with IWC is given in  $\text{g.m}^{-3}$  and  $D_{ge}$  in  $\mu\text{m}$ .  $D_{ge}$  is the generalised effective diameter expressed in terms of the ratio of the mass of particles to their projected area. It has been shown (Fu, 1996) that defining the equivalent diameter  $D_{ge}$  leads to a reduced dependence of extinction with shape. As seen from Eq. (C12), as  $D_{ge}$  is getting smaller, the  $B/D_{ge}$  term becomes preponderant. We then come to an expression which is equivalent to the one for liquid water, where the extinction is inversely proportional to the effective diameter. The value  $D_{gel} = 10B/A$  can be considered as the upper limit to this behaviour with a 10% error. This corresponds to  $D_{gel} = 55 \mu\text{m}$ . When  $D_{ge}$  stays smaller than  $3 \cdot D_{gel}$ , an inverse dependence with  $D_{ge}$  can be considered as a first approximation, and a correction may be further applied using Eq. (C12).

For radar measurements (a wavelength of 3.2 mm is considered here), the scattering at the radar wavelength is due to scattering particles much smaller than the wavelength (Rayleigh scattering). This applies until sizes of about a hundred microns are reached ( $D/\lambda \sim 0.03$ , van de Hulst, 1989). In this case the radar cross section  $\sigma$  is proportional to the 6<sup>th</sup> moment of the PSD. At radar wavelength, the attenuation is depending on vapour and liquid water path. Extinction due to water vapour is small but liquid water can lead to a significant attenuation (Lhermitte, 1994) which may need to be accounted for. Assuming the PSD is given by a single modified gamma distribution in a non precipitating cloud ( $N = N(D/D_m)^\mu \exp(-\Lambda D)$ ), the radar reflectivity  $Z$  is given for water spheres as

$$Z_w = \left( \frac{6LWC}{\pi\rho_w} D_m^3 \right) \frac{(\mu + 6)!}{(\mu + 3)!(\mu + 3)^3} \quad (C13)$$

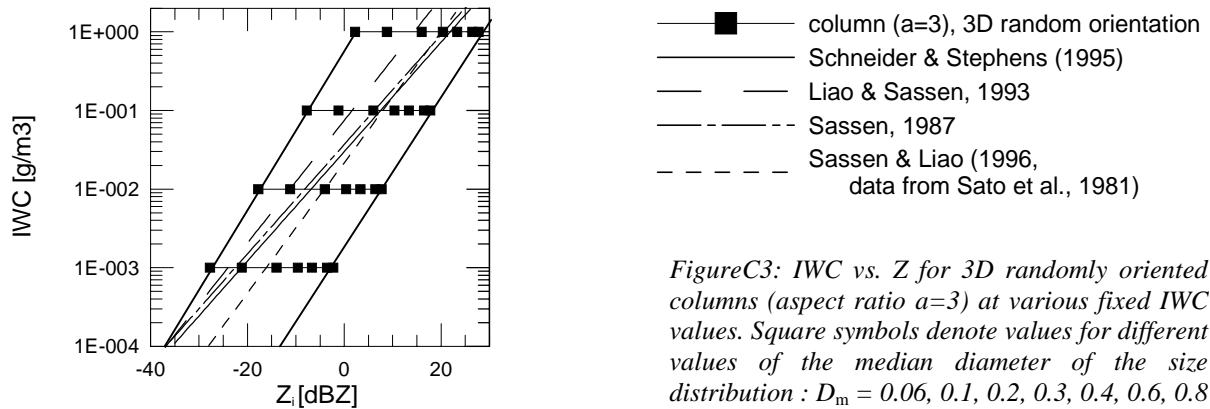
In the case of drizzle occurrence into a cloud, two distinct modes for water cloud and drizzle can be observed in the size distribution. The total reflectivity can then be expressed as the sum of the contributions for the two distributions. Assuming droplet size of drizzle is larger than  $100 \mu\text{m}$  (as compared to  $10 \mu\text{m}$  cloud water droplets) and liquid water in drizzle about ten times smaller than the one related to cloud droplets (ref), the total reflectivity is more than a hundred times (20 dBZ) larger in a drizzling cloud keeping all other microphysical properties constant. Accounting for this contribution may thus introduce further constraints in the analysis.

For radar measurements in ice particles, the reflectivity  $Z_e$  is measured with reference to water and expresses as:

$$Z_e = K^2 Z_i = \frac{|K_i|^2}{\rho_i |K_w|^2} M_6 \quad (C14)$$

where  $K_i$  and  $K_w$  are the refractive coefficients for ice and water, respectively, and  $\rho_i$  is the density of solid ice.  $K_j = \frac{m_j^2 - 1}{m_j^2 + 2}$  in which  $m_j$  is the dielectric constant of water ( $j=w$ ) or ice ( $j=i$ ).

Numerical simulations made at GKSS (Lemke & Quante, 1999) using the Discrete Dipole Approximation (DDA) are reported in Fig. 1 for different sizes assuming an ensemble of randomly oriented crystals having a gamma size distribution. It is observed that the dominant factor controlling the reflectivity is the median size (if analysed as a function of volume. i.e. size is given with regard to volume-equivalent sphere).



FigureC3: IWC vs.  $Z_e$  for 3D randomly oriented columns (aspect ratio  $a=3$ ) at various fixed IWC values. Square symbols denote values for different values of the median diameter of the size distribution :  $D_m = 0.06, 0.1, 0.2, 0.3, 0.4, 0.6, 0.8$  mm. IWC- $Z_e$  relations from literature have been added for comparison. See text for details.

From a power law adjustment on the reflectivity, the dependence with IWC at a given median diameter is seen to be linear  $Z_e \sim IWC$  as for water clouds. As seen from Figure C2, at given IWC values the reflectivity is rapidly decreasing with the median diameter of the size distribution. Assuming a gamma size distribution, it can be shown that the generalised effective diameter and the median diameters are proportional. The dependence of  $Z_e$  with  $D_{ge}$  can thus be represented by a power function of diameter  $Z_e \sim D_{ge}^p$ . From the simulations, the exponent  $p$  is not observed to vary much as a function of the ice water content. It is about 20 % smaller than the value  $p=3$  obtained for water spheres. It is also smaller than values derived from simulations by Wang and Sassen (2002) for a 35 GHz radar wavelength.

In order to keep a general formulation, we will thus write the radar reflectivity as in Wang and Sassen (2002) :

$$Z_e = C \frac{IWC}{\rho} D_{ge}^p \quad (C15)$$

with different values of constants  $C$  and  $p$ .  $C$  will be adjusted to the measurements (see further section). The analysis thus depends on the value of  $p$  chosen. Temperature and lidar depolarisation in semi-transparent clouds is used for setting the best value of  $p$ .

We have considered here the generalised effective diameter of the particles, which means we have accounted for mass and projected area. The ice density which is depending on size for larger particles (see Francis et al., 1998 for example), is thus somewhat accounted for, and we will keep the ice density constant.

For comparison, various IWC-Z relations derived from theoretical models (Schneider & Stephens, 1995) or aircraft measurements of size distributions combined with appropriate scattering calculations (Sassen, 1987; Liao & Sassen, 1994; Sassen & Liao, 1996) have been included. We have also reported in Figure 1 a linear Z~IWC relation for the two extreme diameters. One can see that the the Z-IWC slope obtained from the DDA analysis is larger as any of the other ones. But it is a realistic feature that those literature relations correspond at low reflectivity with the theoretical values for small median sizes whereas for increasing reflectivity the overlap shifts to larger median sizes. A realistic fit of the theoretically derived IWC-Z pairs should take in consideration the increase of the median size with increasing reflectivity.

Assuming the contribution of drizzle is small, relationships given by Eqs (C12) and (C15) can be inverted to derive the effective diameter and ice (liquid) water content from lidar extinction  $\alpha$  and radar reflectivity Z. As discussed above we can use Eq (C12) simplified as a first approximation, *a priori* assuming the effective diameter is small, which give

$$LWC, IWC \propto \alpha^{p/(P+1)} Z^{1/(P+1)} \quad (C16)$$

$$D_e = f(\mu) \left[ \frac{Z}{\alpha} \right]^{1/(1+p)}$$

From Eq. (C16), one can see that the errors on extinction coefficient and reflectivity will translate on errors in water content and diameters so that

$$\frac{\delta LWC}{LWC}, \frac{\delta IWC}{IWC} = \frac{p}{p+1} \left| \frac{\delta \alpha}{\alpha} \right| + \frac{1}{p+1} \left| \frac{\delta Z}{Z} \right| + \frac{\delta p}{p+1} \text{Ln}(Z) + \frac{\delta p}{(p+1)^2} \text{Ln}(\alpha) \quad (C17)$$

$$\frac{\delta D_e}{D_e} = \frac{1}{p+1} \left| \frac{\delta \alpha}{\alpha} \right| + \frac{1}{p+1} \left| \frac{\delta Z}{Z} \right| + \frac{\delta p}{p+1} \text{Ln} \left( \frac{Z}{\alpha} \right)$$

to which a bias due to the error on the  $\mu$  parameters is to be added. As  $p > 1$ , the impact of errors is thus reduced on effective diameter, which can be more accurately retrieved. Use of equations (C12) and (C15) allow to refine estimation. In all cases, the analytical approach implies that a correction for transmission losses is made for lidar and radar signal and requires an exact calibration for both measurements. Furthermore multiple scattering needs to be corrected in lidar signal analysis as it appears as a larger value of transmission (Platt, 1973). An analytical relationship between backscattering and extinction coefficients is used to derive the extinction coefficient from the attenuated backscatter coefficient (Platt, 2002).

## ANNEX D

### RETRIEVAL OF CLOUD DYNAMICAL PROPERTIES (CETP)

The method to recover the dynamic properties of clouds relies upon the combination of the 40° fore and nadir beams of the dual-beam cloud radar. For each beam direction (azimuth  $a$ , elevation  $el$ , see Figure D1) the radial velocity  $V_r$  at a given range  $r$  may be expressed as a function of the horizontal wind component parallel to the aircraft heading ( $V_{//}$ , positive in the direction of the heading) and of the sum ( $Vt+w$ ) of terminal fall speed of the hydrometeors and vertical air velocity (velocity is positive upward) :

$$V_r(r) = V_{//}(r) \delta \cos(el) + (Vt(r) + w(r)) \sin(el) \quad (D1)$$

where  $\delta = +1$  when the antenna points in the heading direction,  $\delta = -1$  when it points in the opposite direction (this latter configuration happens for the nadir beam when the aircraft nose points downward, i.e. the pitch is  $<0$ ).

First the radial velocities and radar pointing angles are corrected for several effects : the pointing angles are corrected for the aircraft pitch, roll, and drift following the procedure described in Lee et al. (1994); the projection of the aircraft ground speed along the beams is removed from the Doppler measurements, and the radial velocities are unfolded using the in-situ wind sensor as a reference for the first gate, a gate-to-gate correction is then applied for the next gates, allowing a maximum wind shear from one gate to the next (for further details, see Protat et al. 1997); the gates contaminated by ground echoes and below the ground are removed. Finally, radar beams for which the absolute value of the aircraft roll is greater than 1° are removed, in order to minimize errors due to the projection of the cross-track horizontal wind component onto the radar beams, which is neglected in the method described hereafter. It is important to mention that the flight plans were designed in such a way that we flew along the flight-level wind. If a cross-track component of 5 ms<sup>-1</sup> is considered, the projection onto the radar beams would lead to a 0.08 ms<sup>-1</sup> peak error for a 1° roll. Larger errors can be expected in cases of strong vertical wind shear.

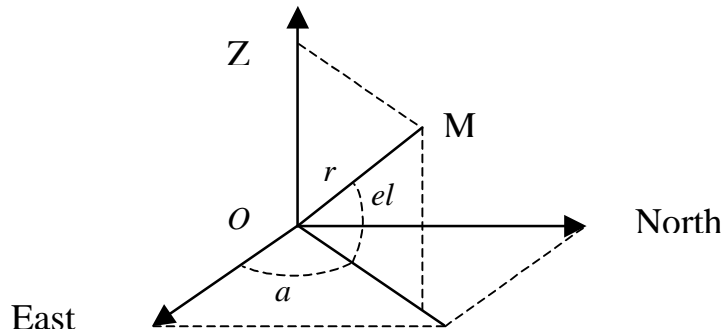


*Figure D1: Definition of the azimuth  $\alpha$ , elevation  $el$ , and range  $r$  in the earth-relative coordinate system. The radar is located at its origin  $O_a$ .*

In a second step the data from each antenna are reorganized into a two-dimensional Cartesian grid. A trade-off for the grid size has been searched, in order to keep the best resolution for the retrieved two-dimensional field on the one hand, but to filter out the measurement noise and errors introduced by the roll angle on the other hand. A grid mesh of 300 m horizontally and 100 m vertically is used in what follows. Let us recall that due to aircraft motion, the horizontal resolution of our measurements is around 20 m horizontally (for a typical ground speed of 120 ms<sup>-1</sup>), and 60 m along the beams. This leads to an average of 30 points at most in

each grid. The mean roll angle is computed in order to monitor the expected accuracy of the retrieved two-dimensional field in each grid.

The method used for the retrieval of the two wind components  $V_{//}$  and  $(V_{t+w})$  simply consists in solving for each grid the set of two equations derived from (D1), which leads to the following equations :

$$V_{//} = \frac{V_1 \sin(el_2) - V_2 \sin(el_1)}{\cos(el_2)\sin(el_1) - \delta \cos(el_1)\sin(el_2)} \quad (D2)$$

$$V_{t+w} = \frac{V_2 \delta \cos(el_1) - V_1 \cos(el_2)}{\cos(el_2)\sin(el_1) - \delta \cos(el_1)\sin(el_2)} \quad (D3)$$

where subscripts 1 and 2 refer to the nadir and 40° fore measurements, respectively.

Up to here, the terminal fall velocity and vertical wind component are not separated. In order to estimate the terminal fall velocity, a statistical approach is proposed in what follows, as already discussed for frontal cyclones in Protat et al. (2000, 2002). Within weakly-precipitating clouds, the vertical air motions are generally small, even at small scales of motion, as opposed to the case of convective systems. In any case, however, the vertical air motions are not negligible with respect to the terminal fall speed, but if the analysis is made over a long time span (a whole aircraft mission, for instance), then *the mean vertical air motions should statistically vanish with respect to the mean terminal fall speed*, which is much less fluctuating. A statistical power-law relationship between the terminal fall speed and radar reflectivity may therefore be derived from this statistical approach. This hypothesis has been recently validated in the case of frontal cyclones sampled during FASTEX (Protat et al. 2002). A more thorough validation of this assumption will be performed in a near future using high-resolution numerical simulations of cirrus clouds.

